N-body simulations with a cosmic vector for dark energy

Edoardo Carlesi,[1]★ Alexander Knebe,[1] Gustavo Yepes,[1] Stefan Gottlöber,[2]
Jose Beltrán Jiménez[3,4] and Antonio L. Maroto[5]

[1]*Departamento de Física Teórica, Universidad Autónoma de Madrid, 28049 Cantoblanco, Madrid, Spain*
[2]*Leibniz Institut für Astrophysik, An der Sternwarte 16, 14482 Potsdam, Germany*
[3]*Institute de Physique Théorique and Center for Astroparticle Physics, Université de Genève, 24 quai E. Ansermet, 1211 Genève, Switzerland*
[4]*Institute of Theoretical Astrophysics, University of Oslo, 0315 Oslo, Norway*
[5]*Departamento de Física Teórica, Universidad Complutense de Madrid, 28040 Madrid, Spain*

ABSTRACT

We present the results of a series of cosmological *N*-body simulations of a vector dark energy (VDE) model, performed using a suitably modified version of the publicly available GADGET-2 code. The set-ups of our simulations were calibrated pursuing a twofold aim: (1) to analyse the large-scale distribution of massive objects and (2) to determine the properties of halo structure in this different framework. We observe that structure formation is enhanced in VDE, since the mass function at high redshift is boosted up to a factor of 10 with respect to Λ cold dark matter (ΛCDM), possibly alleviating tensions with the observations of massive clusters at high redshifts and early reionization epoch. Significant differences can also be found for the value of the growth factor, which in VDE shows a completely different behaviour, and in the distribution of voids, which in this cosmology are on average smaller and less abundant. We further studied the structure of dark matter haloes more massive than $5 \times 10^{13}\,h^{-1}\,\mathrm{M_\odot}$, finding that no substantial difference emerges when comparing spin parameter, shape, triaxiality and profiles of structures evolved under different cosmological pictures. Nevertheless, minor differences can be found in the concentration–mass relation and the two-point correlation function, both showing different amplitudes and steeper slopes. Using an additional series of simulations of a ΛCDM scenario with the same Ω_M and σ_8 used in the VDE cosmology, we have been able to establish whether the modifications induced in the new cosmological picture were due to the particular nature of the dynamical dark energy or a straightforward consequence of the cosmological parameters. On large scales, the dynamical effects of the cosmic vector field can be seen in the peculiar evolution of the cluster number density function with redshift, in the shape of the mass function, in the distribution of voids and on the characteristic form of the growth index $\gamma(z)$. On smaller scales, internal properties of haloes are almost unaffected by the change of cosmology, since no statistical difference can be observed in the characteristics of halo profiles, spin parameters, shapes and triaxialities. Only halo masses and concentrations show a substantial increase, which can, however, be attributed to the change in the cosmological parameters.

Key words: galaxies: haloes – cosmology: theory – dark matter.

1 INTRODUCTION

During the last 12 years, a large amount of cosmological high-precision data on Type Ia supernovae (SNeIa; see Riess et al. 1998; Perlmutter et al. 1999; Guy et al. 2010), cosmic microwave background (CMB) anisotropies (Larson et al. 2011; Sherwin et al. 2011), weak lensing (Huterer 2010), baryon acoustic oscillations (Beutler et al. 2011) and large-scale structure surveys (Abazajian et al. 2009) has provided evidence that the Universe we live in is of a flat geometry and undergoing an accelerated expansion. These observations motivate our belief in the existence of a ubiquitous fluid called dark energy (DE) that, by the exertion of a negative pressure, counters and eventually overcomes the gravitational attraction that would otherwise dominate the evolution of our Universe. The simplest explanation to the nature of this fluid is found in the

★E-mail: edoardo.carlesi@uam.es

standard model of cosmology Λ cold dark matter (ΛCDM), where
the role of the DE is played by a cosmological constant Λ obeying
the equation of state $p_\Lambda = -\rho_\Lambda$. Although perfectly consistent with
all the aforementioned observations, ΛCDM still lacks an appeal
from a purely theoretical point of view. In fact, if we believe the
cosmological constant to be the zero-point energy of some funda-
mental quantum field, its introduction in the Friedmann equations
requires a fine tuning of several tens of orders of magnitude (de-
pending on the energy scale we choose to be fundamental in our
theory), spoiling the naturalness of the whole ΛCDM picture.

Another issue we encounter when dealing with the standard cos-
mological model is the so-called *coincidence problem*, i.e. the dif-
ficulty to explain in a natural way the fact that today's matter and
DE densities have a comparable value although they evolved in a
completely different manner throughout most of the history of the
universe.

In an attempt to overcome these two difficulties of ΛCDM,
Jimenez & Maroto (2009) introduced the vector dark energy (VDE)
model, where a cosmic vector field plays the role of a dynamical
DE component, replacing the cosmological constant Λ. Besides
being compatible with SN observations and CMB precision mea-
surements, this scenario has the same number of free parameters as
ΛCDM. Moreover, the initial value of the vector field (which is of
the order of $10^{-4}M_{\rm p}$,[1] a scale that could arise naturally in inflation)
and its global dynamics ensure the model to overcome the standard
model's naturalness problems. In the present work, we study the
impact of this VDE model on structure formation and evolution by
means of a series of cosmological *N*-body simulations, analysing
the effects of this alternative cosmology in the deeply non-linear
regime and highlighting its imprints on cosmic structures, in par-
ticular emphasizing the differences emerging with respect to the
standard ΛCDM model. To be able to disentangle the effects due to
the different parameters from those induced by the different dynam-
ics of the background in VDE cosmology, we have also run a set
of simulations for a ΛCDM-vde cosmology, i.e. a model that em-
beds VDE parameters (presented in Section 2) in a standard ΛCDM
picture.

Although ruled out by current cosmological constraints, this
model provides none the less an interesting case study that allows
us to shed light on the effects of these two cosmological parameters
on structure formation in the VDE model.

The paper is organized as follows. In Section 2, we briefly intro-
duce the VDE model, discussing its most important mathematical
and physical characteristics. In Section 3, we describe the set-up
as well as the modifications to the code and the initial conditions
necessary to run the *N*-body simulation. In Sections 4 and 5, we will
present a detailed analysis of the results, focusing on the main dif-
ferences of the VDE models from the standard ΛCDM cosmology,
first analysing the large-scale structure and then (cross-)comparing
properties of dark matter haloes. A short summary of the results
obtained and a discussion on their implications are then presented
in Section 6.

2 THE MODEL

In this section, we will provide the basic mathematical and physical
description of the VDE model. For more details and an in-depth
discussion on the results obtained and their derivation, we refer
the reader to Beltrán Jiménez & Maroto (2008). The action of the

[1] $M_{\rm p}$ being the Planck mass.

proposed VDE model can be written as

$$S = \int d^4x \sqrt{-g} \left[-\frac{R}{16\pi G} - \frac{1}{4}\boldsymbol{F}_{\mu\nu}\boldsymbol{F}^{\mu\nu} \right.$$
$$\left. -\frac{1}{2}(\nabla_\mu \boldsymbol{A}^\mu)^2 + \boldsymbol{R}_{\mu\nu}\boldsymbol{A}^\mu \boldsymbol{A}^\nu \right], \quad (1)$$

where $\boldsymbol{R}_{\mu\nu}$ is the Ricci tensor, $R = \boldsymbol{g}^{\mu\nu}\boldsymbol{R}_{\mu\nu}$ the scalar curvature and
$\boldsymbol{F}_{\mu\nu} = \partial_\mu \boldsymbol{A}_\nu - \partial_\nu \boldsymbol{A}_\mu$. This action can be interpreted as a Maxwell
term for a vector field supplemented with a gauge-fixing term and
an effective mass provided by the Ricci tensor. It is interesting to
note that the vector sector has neither free parameters nor potential
terms, *G* being the only dimensional constant of the theory. This
is one of the main differences of this model with respect to those
based on scalar fields, which need the presence of potential terms
to be able to lead to late-time accelerated expansion.

The classical equations of motion derived from the action (1) are
the Einstein and vector field equations given by

$$\boldsymbol{R}_{\mu\nu} - \frac{1}{2}R\boldsymbol{g}_{\mu\nu} = 8\pi G(\boldsymbol{T}_{\mu\nu} + \boldsymbol{T}^A_{\mu\nu}), \quad (2)$$

$$\Box \boldsymbol{A}_\mu + \boldsymbol{R}_{\mu\nu}\boldsymbol{A}^\nu = 0, \quad (3)$$

where $\boldsymbol{T}_{\mu\nu}$ is the conserved energy–momentum tensor for matter
and radiation (and/or other possible components present in the
Universe) and $\boldsymbol{T}^A_{\mu\nu}$ is the energy–momentum tensor coming from
the vector field sector (and that is also covariantly conserved). In the
following, we shall solve the equations of the vector field during
the radiation and matter eras, in which the contribution of DE is
supposed to be negligible. In those epochs, the geometry of the uni-
verse is well described by the flat Friedmann–Lemaître–Robertson–
Walker metric:

$$ds^2 = dt^2 - a(t)^2 d\boldsymbol{x}^2. \quad (4)$$

For the homogeneous vector field, we shall assume, without lack of
generality, the form $A_\mu = (A_0(t), 0, 0, A_z(t))$, so that the correspond-
ing equations read

$$\ddot{A}_0 + 3H\dot{A}_0 - 3\left(2H^2 + \dot{H}\right)A_0 = 0, \quad (5)$$

$$\ddot{A}_z + H\dot{A}_z - 2\left(\dot{H} + 3H^2\right)A_z = 0, \quad (6)$$

where $H = \dot{a}/a$. These equations can be easily solved for a power-
law expansion with $H = p/t$, in which case we obtain the following
solutions:

$$A_0(t) = A_0^+ t^{\alpha_+} + A_0^- t^{\alpha_-}, \quad (7)$$

$$A_z(t) = A_z^+ t^{2p} + A_z^- t^{1-3p}, \quad (8)$$

with $\alpha_\pm = \frac{1}{2}(1-3p\pm\sqrt{33p^2 - 18p + 1})$ and $A_0^\pm$ and $A_z^\pm$ constants
of integration. Thus, in the radiation-dominated epoch ($p = 1/2$) we
have the growing modes $A_0 = $ constant and $A_z \propto t$, whereas for
the matter-dominated epoch ($p = 2/3$) we have $A_0 \propto t^{(-3+\sqrt{33})/6}$
and $A_z \propto t^{4/3}$. Concerning the energy densities, the corresponding
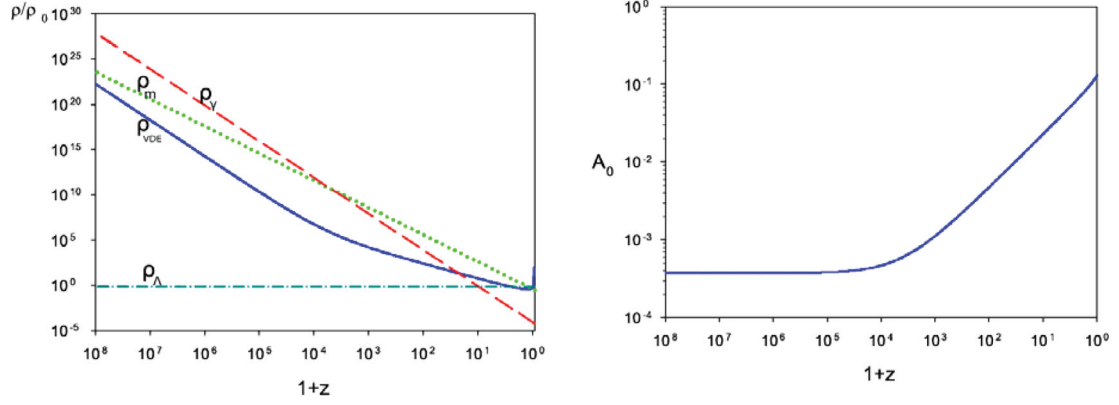expressions are given by

$$\rho_{A_0} = \frac{3}{2}H^2 A_0^2 + 3H A_0 \dot{A}_0 - \frac{1}{2}\dot{A}_0^2, \quad (9)$$

$$\rho_{A_z} = \frac{1}{2a^2}\left(4H^2 A_z^2 - 4H A_z \dot{A}_z + \dot{A}_z^2\right). \quad (10)$$

At this point, it is interesting to note that when we insert the full
solution for A_z given in (8) in its corresponding energy density, we
obtain

$$\rho_{A_z} = \frac{\left(A_z^-\right)^2}{2a^8}(25p^2 - 10p + 1), \quad (11)$$

Figure 1. Left-hand plot: evolution of the energy densities. Dashed (red) for radiation, dotted (green) for matter and solid (blue) for VDE. We also show for comparison the cosmological constant energy density in dot–dashed line. We see the scaling behaviour of the cosmic vector in the early universe and the rapid growth of its energy density contribution at late times when approaching the final singularity. Right-hand plot: evolution of the temporal component of the vector field where we see that it takes a constant value at very high redshifts so that the cosmological evolution is insensitive to the precise redshift at which we set the initial value of the cosmic vector.

so that the mode A_z^+ does not contribute to the energy density. That way, even though A_z grows with respect to A_0, the corresponding physical quantity, i.e. its energy density, decays with respect to that of the temporal component. It is easy to check that the ratio ρ_{A_z}/ρ_{A_0} decays as a^{-4} in the radiation era and as $a^{-6.37}$ in the matter era, so that the energy density of the vector field becomes dominated by the contribution of the temporal component. That justifies neglecting the spatial components and dealing uniquely with the temporal one.

On the other hand, the potential large-scale anisotropy generated by the presence of spatial components of the vector field is determined by the relative difference of pressures in different directions $p_\parallel$ and $p_\perp$, which is given by

$$p_\parallel - p_\perp = \frac{3}{a^2}\left(4H^2 A_z^2 - 4H A_z \dot{A}_z + \dot{A}_z^2\right). \tag{12}$$

This expression happens to be proportional to ρ_{A_z} so that we have that $(p_\parallel - p_\perp)/\rho_A$ will decay as the universe expands in the same manner as ρ_{A_z} and the large-scale isotropy of the universe suggested by CMB observations is not spoiled. Hence, in the following we shall neglect the spatial components of the vector field and uniquely consider the temporal one, since it gives the dominant contribution to the energy–momentum tensor of the vector field. However, we should emphasize here that this does not result in effectively having a scalar field. As commented before, for a minimally coupled scalar field, one needs to introduce a certain potential (that will depend on some dimensional parameters) to have accelerated expansion, whereas in the VDE model we get accelerated solutions with only kinetic terms and without introducing any new dimensional parameter.

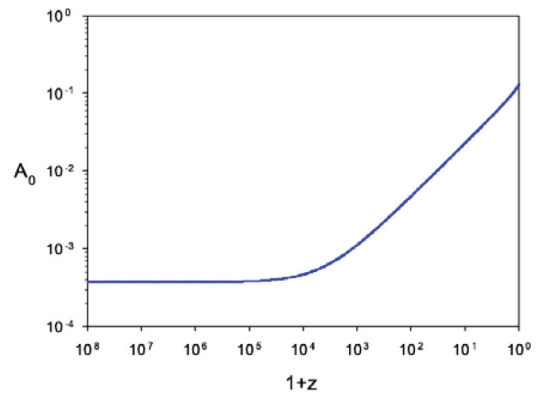The energy density of the vector field is given by

$$\rho_A = \rho_{A0}(1+z)^\kappa, \tag{13}$$

with $\kappa = 4$ in the radiation era and $\kappa = (9 - \sqrt{33})/2 \simeq -1.63$ in the matter era. We can also calculate the effective equation of state for DE as

$$w_{\mathrm{DE}} = \frac{p_A}{\rho_A} = \frac{-3\left(\frac{5}{2}H^2 + \frac{4}{3}\dot{H}\right)A_0^2 + H A_0 \dot{A}_0 - \frac{3}{2}\dot{A}_0^2}{\frac{3}{2}H^2 A_0^2 + 3H A_0 \dot{A}_0 - \frac{1}{2}\dot{A}_0^2}. \tag{14}$$

Again, using the approximate solutions in (7), we obtain

$$w_{\mathrm{DE}} = \begin{cases} \frac{1}{3} & \text{radiation era} \\ \frac{3\sqrt{33}-13}{\sqrt{33}-15} \simeq -0.457 & \text{matter era.} \end{cases} \tag{15}$$

From the evolution of the energy density of the vector field, we see that it scales as radiation at early times, so that $\rho_A/\rho_R = $ constant. However, when the Universe enters its matter era, ρ_A starts growing relative to ρ_M, eventually overcoming it at some point, at which the DE vector field would become the dominant component. From that point on, we cannot obtain analytic solutions to the field equations and we need to numerically solve the corresponding equations. In Fig. 1, we show such a numerical solution to the exact equations, which confirms our analytical estimates in the radiation and matter eras. Note that, since A_0 is constant during the radiation era, the solutions do not depend on the precise time at which we specify the initial conditions as long as we set them well inside the radiation epoch. Thus, once the present value of the Hubble parameter H_0 and the constant A_0 during radiation (which indirectly fixes the total matter density Ω_M) are specified, the model is completely determined. In other words, this model contains the same number of parameters as ΛCDM, i.e. the minimum number of parameters of any cosmological model with DE.

Not only does the VDE model have the minimum required number of parameters, but also it allows us to alleviate the so-called naturalness or coincidence problems that most DE models have. This is so because the required value for the constant value that the vector field takes in the early universe happens to be $\sim 10^{-4} M_p$. This value, besides being relatively close to the Planck scale, could naturally arise from quantum fluctuations during inflation, for instance. On the other hand, the fact that the energy density of the vector field scales as radiation in the early universe also goes in the right direction of alleviating the aforementioned problems because the fraction of dark energy during that period remains constant. Moreover, the said fraction is $\Omega_A^{\mathrm{early}} \equiv \rho_A/\rho_R \simeq 10^{-6}$, which, again, is in agreement with the usual magnitude of the quantum fluctuations produced during inflation.

After DE starts dominating, the equation of state abruptly falls towards $w_{\mathrm{DE}} \to -\infty$ as the Universe approaches a finite time t_{end}. As shown in Fig. 2, during the cosmological evolution, the equation of state crosses the so-called phantom divide line, so that we have $w_{\mathrm{DE}}(z = 0) < -1$. The final stage of the universe in this model is a singularity usually called Type III or Big Freeze, in which the scale factor remains finite, but the Hubble expansion rate, the energy density and the pressure diverge. This is a distinct feature of the VDE model as compared to quintessence fields for which the
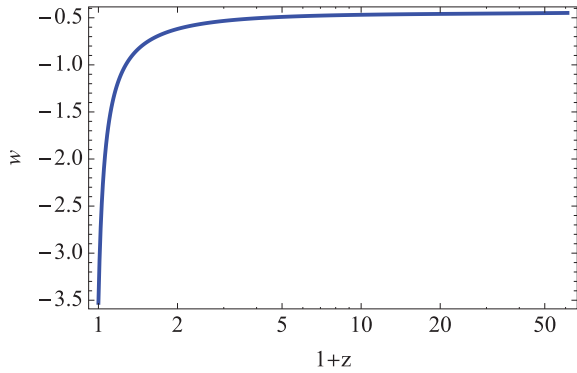
Figure 2. Evolution of DE equation of state where we can see the crossing of the phantom divide line and its evolution towards $-\infty$ as the final singularity is approached.

Table 1. *N*-body settings and cosmological parameters used for the GADGET-2 simulations. The two $500\,h^{-1}$ Mpc and the two $1\,h^{-1}$ Gpc have the same initial random seed (in order to allow for a direct comparison of the halo properties) and starting redshift $z_{\text{start}} = 60$. The number of particles in each run was fixed at 512^3. The box size B is given in units of h^{-1} Mpc and the particle mass (m_{p}) in $10^{11}\,h^{-1}\,\text{M}_\odot$.

Simulation	Ω_{m}	Ω_{DE}	σ_8	h	B	m_{p}
$2 \times$VDE-0.5	0.388	0.612	0.83	0.62	500	1.00
$2 \times$VDE-1	0.388	0.612	0.83	0.62	1000	8.02
ΛCDM-0.5	0.27	0.73	0.8	0.7	500	0.69
ΛCDM-1	0.27	0.73	0.8	0.7	1000	5.55
ΛCDM-0.5vde	0.388	0.612	0.83	0.7	500	1.00
ΛCDM-1vde	0.388	0.612	0.83	0.7	1000	8.02

equation of state is restricted to be > -1 so that no crossing of the phantom divide line is possible. In fact, for a DE model based on scalar fields, one needs either non-standard kinetic terms involving higher derivative terms in the action or the presence of several interacting scalar fields to achieve a transition from $w > -1$ to a phantom behaviour ($w < -1$). In either case, non-linear derivative interactions or multiple scalar field scenarios, additional degrees of freedom are introduced, whereas the VDE model is able to obtained the mentioned transition with only the degree of freedom given by the temporal component of the vector field.

Note that in the VDE model the present value of the equation of state parameter $w_0 = -3.53$ is radically different from that of a cosmological constant [cf. Fig. 1, where the redshift evolution of $w(z)$ is shown in the range of our simulations]. The values of other cosmological parameters also differ importantly from those of ΛCDM (see Table 1). Despite this fact, VDE is able to simultaneously fit SNe and CMB data with comparable goodness to ΛCDM (Beltrán Jiménez & Maroto 2008; Beltrán Jiménez, Lazkoz & Maroto 2009).

In particular, for CMB,[2] the χ^2 for the best-fitting parameters for ΛCDM is 48.3, whereas for the VDE model we obtain $\chi^2 = 51.8$ for the parameters used to run our simulations. Thus, even though the equation of state evolution is the one shown in Fig. 2, the VDE model provides good fits to observations, as shown in Fig. 3.

This might seem to be surprising if we note that the present equation of state for the VDE model is $w_0 = -3.53$, which is far from
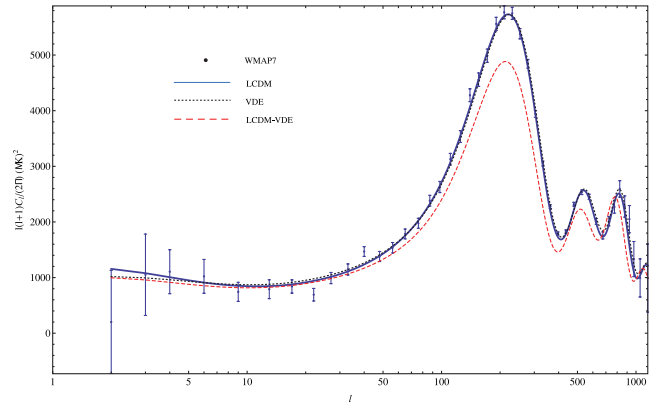
Figure 3. ΛCDM and VDE best-fitting values for the CMB spectrum versus *WMAP*7 data, showing the viability of VDE cosmology. The same curve is also shown for a ΛCDM-vde cosmology, which is clearly ruled out.

the usual constraints on this parameter obtained from cosmological observations. Such constraints are usually obtained by assuming a certain parametrization for the time variation of the DE equation of state. However, the different parametrizations used are normally such that ΛCDM is included in the parameter space. If we look at Fig. 2, we can see that the evolution of the equation of state for the VDE model crucially differs from those of ΛCDM or quintessence models and, indeed, it cannot be properly described by the most popular parametrizations. This means that we cannot directly apply the existing constraints to the VDE model, but a direct comparison of its predictions to observations is required.

As a final remark, in the simulations we will not include inhomogeneous perturbations of the vector field, but only the effects of having a different background expansion will be considered.

In Fig. 4, we show the matter power spectrum for both ΛCDM and VDE models. The differences can be ascribed to the fact of having different cosmological parameters that change the normalization
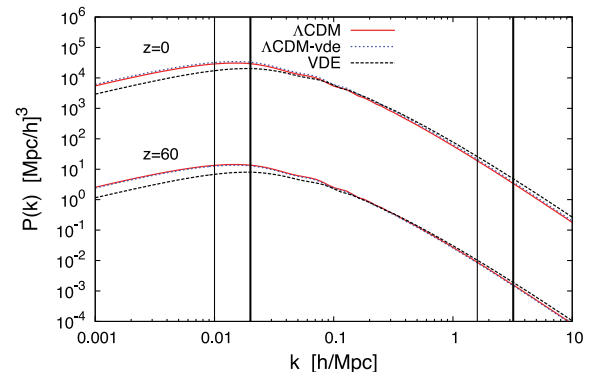
Figure 4. Linear matter overdensity power spectra at $z = 0$ and 60 for VDE, ΛCDM and ΛCDM-vde plotted versus wavenumber k. Vertical solid thick black lines refer to the k-space interval covered by the $500\,h^{-1}$ Mpc simulations, whereas the thin ones refer to the $1\,h^{-1}$ Gpc one. All matter power spectra at $z = 0$ have been normalized to the σ_8 values shown in Table 1 and then rescaled to $z = 60$ via the linear growth factor. We note that for $k < 0.05\,h\,\text{Mpc}^{-1}$, ΛCDM and ΛCDM-vde have more power than VDE, whereas on smaller scales the opposite is true. We also note that due to the different value of σ_8 normalization the ΛCDM-vde $P(k)$ is slightly larger than the ΛCDM one at $z = 0$, while the different growth factor, which is larger in the ΛCDM-vde cosmology, affects the setting of the initial conditions, where the latter power spectrum lies below the former.

and the matter–radiation equality scale k_{eq}, which are the only two differences observed. Note that the transfer function is the same in both cases, since the slopes before and after the k_{eq} are the same, so that we do not expect strong effects at early times which could affect the evolution of density parameters.

3 THE *N*-BODY SIMULATIONS

In this section, we will explain the (numerical) methods used in this work, with a particular emphasis on the necessary modifications of the standard *N*-body and halo-finding algorithms, also describing the procedures followed to test their accuracy and reliability.

3.1 Set-up

The *N*-body simulations presented in this work have been carried out using a suitably modified version of the Tree-PM code GADGET-2 (Springel 2005). It has also been necessary to generate a particular set of initial conditions to consistently account for the VDE-induced modifications to the standard paradigm. In Table 1, we show the most relevant cosmological parameters used in the different simulations. For the VDE model, we have used the value of Ω_M provided by the best fit to SNIa data, whereas the remaining cosmological parameters have been obtained by a fit of the model to the *WMAP*7 data set. For ΛCDM, we used the Multidark Simulation (Prada et al. 2011) cosmological parameters with a *WMAP*7 σ_8 normalization (Larson et al. 2011).

In addition, we also simulated the so-called ΛCDM-vde model, which implements the VDE values for the total matter density Ω_M and fluctuation amplitude σ_8 in an otherwise standard ΛCDM picture.

In particular, we want to be able to determine the impact of the different parameters on cosmological scales, with a particular emphasis on the very large structures and the most massive clusters, where observations are starting to clash with the predictions of the current standard model (see Jee et al. 2009; Baldi & Pettorino 2011; Carlesi et al. 2011; Enqvist, Hotchkiss & Taanila 2011; Hoyle, Jimenez & Verde 2011). Therefore, we need to determine whether the results derived from our VDE simulations can be solely attributed to its extremely different values for the cosmological parameters or actually by the presence of the cosmic vector field. In other words, we want to separate the signatures of the *dynamics*-driven effects from the *parameter*-driven ones, with a focus on large-scale structures, where the imprints are stronger and more clearly connected to the cosmological model. We chose to run a total of eight 512^3 particle simulations summarized in Table 1 and explained below.

(i) Two VDE simulations, i.e. a $500\,h^{-1}$ Mpc and a $1\,h^{-1}$ Gpc box.

(ii) Two ΛCDM simulations with the same box sizes and initial seeds as the VDE runs above.

(iii) Two more VDE simulations with a different random seed, again one in a $500\,h^{-1}$ Mpc and another in a $1\,h^{-1}$ Gpc box (both serving as a check for the influence of cosmic variance).

(iv) Two ΛCDM-vde simulations, one again in a $500\,h^{-1}$ Mpc and another in a $1\,h^{-1}$ Gpc box.

All runs were performed on 64 CPUs using the MareNostrum cluster at the Barcelona Supercomputing Center. Most of the results we will discuss and analyse here are based on the $500\,h^{-1}$ Mpc simulations as they have the better mass resolution. The $1\,h^{-1}$ Gpc runs primarily serve as a confirmation of the results and have already been discussed in Carlesi et al. (2011).

3.2 Code modifications

In the following paragraph, we are going to describe the procedures followed to implement the modifications needed in order to run our *N*-body simulations consistently and reliably. This is in principle a non-trivial issue, since, as described in Section 2, we need to incorporate a large number of different features that affect both the code used for the simulations and the initial conditions.

In particular, we have to handle with care three features that distinguish it from ΛCDM, i.e.

(i) the matter power spectrum $P(k, z)$ (shown in Fig. 4) and its normalization σ_8,
(ii) the expansion history $H(z)$ (see Fig. 5) and
(iii) the linear growth factor $D^+(z)$ (cf. Fig. 6).

Whereas the first and the last points affect the system's initial conditions, the second one enters directly into the *N*-body time integration, and has to be taken into account by a modification of the simulation code.
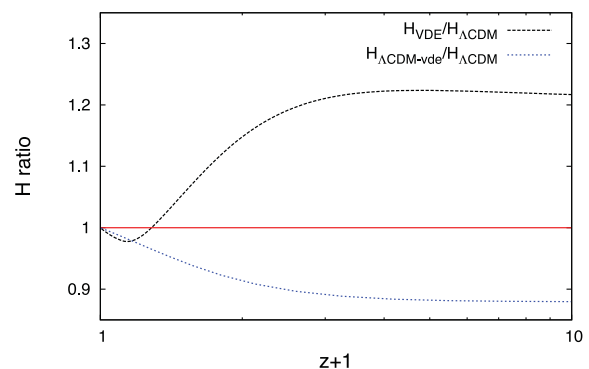
Figure 5. The ratio of the Hubble function $H(a)h^{-1}$ for VDE and ΛCDM-vde to the standard ΛCDM one. At earlier times, VDE undergoes a relatively faster expansion compared to ΛCDM, whereas the opposite is true at smaller z values. On the other hand, ΛCDM-vde cosmology is characterized by a slower relative expansion throughout the whole history of the universe.
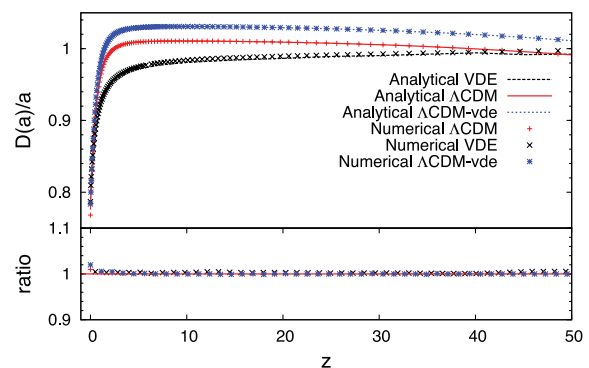
Figure 6. Ratio of the growth function to the expansion factor $D(a)/a$ as obtained from the $500\,h^{-1}$ Mpc box simulations versus the analytical one. The results show an agreement between the theoretical expectation and the numerically computed one within the 2 per cent level. The results from the $1\,h^{-1}$ Gpc box simulations are not shown since they perfectly overlap with the ones presented here.

3.2.1 Initial conditions

To consistently generate the initial conditions for our simulation, first we normalized the perturbation power spectrum depicted in Fig. 4 to the chosen value for σ_8 at $z = 0$. Therefore, we normalized VDE and ΛCDM-vde initial conditions to $\sigma_8 = 0.83$, while for ΛCDM we used the *WMAP*7 value $\sigma_8 = 0.8$. Using the respective linear growth factors, we rescaled the $P(k)$ to the initial redshift $z = 60$, where the particles' initial velocities and positions were computed using the Zeldovich (1970) approximation.

We emphasize here that the main goal of our analysis is to find and highlight the main differences of the VDE picture with respect to the standard one: therefore, the choice of these different normalization parameters has to be understood as unavoidable as long as we want the models under investigation to be *WMAP*7 viable ones. Needless to say, in this regard the ΛCDM-vde cosmology must be considered only as a tool to disentangle parameter-driven effects from the dynamical ones, not being a concurrent cosmological paradigm we want to compare VDE to.

3.2.2 Hubble expansion

As pointed out by Li & Barrow (2011), the expansion history of the universe has a very deep impact on structure formation and in particular the results of an N-body simulation, as it affects directly every single particle through the equations of motion written in comoving coordinates. In Fig. 5, the ratios of the Hubble expansion factors for VDE and ΛCDM-vde to the standard ΛCDM value are shown; we see that different models are characterized by differences up to 20 per cent in the expansion rate. To implement this modification, we replaced the standard computation of $H(a)$ in GADGET-2 with a routine that reads and interpolates from a pre-computed table.

3.3 Code testing

To check the reliability of the modifications introduced into the simulation code and during the generation of the initial conditions, we have confronted the theoretical linear growth factor, computed using the Boltzmann code CAMB (Lewis, Challinor & Lasenby 2000), with the ones derived directly from the simulations.

As shown in Fig. 6, our results yield an agreement within the 1 per cent level, which proves the correctness of our modifications as well as illustrating (again) the differences in structure growth between the models.

We would like to note that for consistency reasons, when calculating both the CAMB and the numerical value for the growth factor, we have used the expression

$$D^+(z) = \sqrt{\frac{P(z, k_0)}{P(z_0, k_0)}},\qquad(16)$$

where k_0 is a fixed scale within the linear regime and z_0 is the initial redshift of the simulation.

3.4 Halo finding

In order to identify haloes in our simulation, we have run the open source MPI+OpenMP hybrid halo finder AHF[3] described in detail in Knollmann & Knebe (2009). AHF is an improvement of the

---

[3] AHF stands for Amiga Halo Finder, to be downloaded freely from http://www.popia.ft.uam.es/AMIGA

MHF halo finder (Gill, Knebe & Gibson 2004) and has been extensively compared against practically all other halo-finding methods in Knebe et al. (2011). AHF locates local overdensities in an adaptively smoothed density field as prospective halo centres. For each of these density peaks, the gravitationally bound particles are determined. Only peaks with at least 20 bound particles are considered as haloes and retained for further analysis.

However, the determination of the mass requires a bit more elaboration as it is computed via the equation

$$M(R) = \Delta \times \rho_{\rm c}(z) \times \frac{4\pi}{3} R^3 ,\qquad(17)$$

where we applied $\Delta = 200$ as the overdensity threshold and $\rho_{\rm c}(z)$ refers to the critical density of the universe at redshift z. In this way, $M(R)$ is defined as the total mass contained within a radius R, corresponding to the point where the halo matter density $\rho(r)$ is Δ times the critical value $\rho_{\rm c}$. While using this relation particular care has to be taken when considering the definition of the critical density

$$\rho_{\rm c}(z) = \frac{3H^2(z)}{8\pi G}\qquad(18)$$

because it involves the Hubble parameter that differs substantially at all redshifts in the two models. This means that, identifying the halo masses, we have to take into account the fact that the value of $\rho_{\rm c}(z)$ changes from ΛCDM to VDE. This has been incorporated into and taken care of in the latest version of AHF where $H_{\rm VDE}(z)$ is being read in from a pre-computed table, too.

We finally need to mention that we checked that the objects obtained by this (virial) definition can be compared across different cosmological models and using different mass definitions. To this extent, we studied the ratio between two times kinetic over potential energy $\eta = 2T/|U|$, confirming that at each redshift under investigation here the distributions of η in ΛCDM and VDE are actually comparable (not presented here though), meaning that the degree of virialization (which should be guaranteed by equation 17) is in fact similar. We therefore conclude that our adopted method to define halo mass (and edge) in the VDE model leads to unbiased results and yields objects in the same state of equilibrium as is the case for the ΛCDM haloes. Please note that this test does not guarantee that all our objects are in fact virialized; it merely assures us that the degree of virialization is equivalent. We will come back to this issue later when selecting only equilibrated objects.

4 LARGE-SCALE STRUCTURE AND GLOBAL PROPERTIES

In the following section, we will discuss the global properties of large-scale structures identified in our simulations. Using all of our sets of simulations for ΛCDM, ΛCDM-vde and VDE, we will disentangle parameter-driven effects from those due to the different dynamics of the background expansion, which uniquely characterize VDE and therefore are worth pointing out in the process of model selection.

4.1 Density distribution

In Fig. 7, we show the colour-coded density field for the particle distribution at redshift $z = 0$, for a $120 \times 120 \, h^{-1}$ Mpc^2 slice at the box centre for the three $500 \, h^{-1}$ Mpc simulations projected on the x–z plane. As expected, we observe that the most massive structures' spatial positions match in the three simulations, although in the
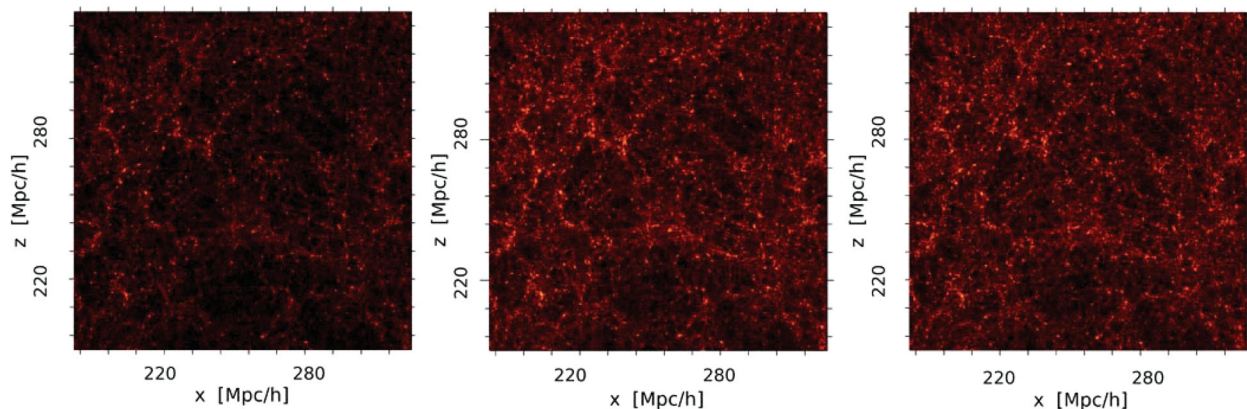
Figure 7. Projected density for ΛCDM, ΛCDM-vde and VDE showing a $120 \times 120 \, h^{-2} \, \text{Mpc}^2$ slice at the box centre in the $500 \, h^{-1}$ Mpc box at $z = 0$ projected on the x–z plane. Bright areas are associated with matter, whereas underdense regions are denoted by darker, black spots in the projected box. Results for the VDE-1, ΛCDM-1 and ΛCDM-vde-1 simulations are not shown since the colour coding does not provide useful insights on the different clustering patterns on smaller scales.

ΛCDM-vde and VDE observations we see a large overabundance of objects with respect to ΛCDM, as we could expect due to the higher Ω_M. This observation will be confirmed on more quantitative grounds in the analysis carried out in the following sections, especially when referring to the study of the cumulative mass function.

4.2 Matter power spectrum

In Fig. 8, we show the dark matter power spectrum $P(k)$ at redshifts $z = 0, 1, 3, 4$ computed for the VDE-0.5, ΛCDM-0.5 and ΛCDM-vde-0.5 simulations. For clarity, we do not show the $1 \, h^{-1}$ Gpc simulations; however, we have checked their consistency with the $500 \, h^{-1}$ Mpc runs. We note that at all redshifts the differences already seen in the input power spectra are preserved (cf. Fig. 4), meaning that the VDE model has less power than ΛCDM on the large scales, whereas the opposite is true for small scale. This particular shape of the $P(k)$ is a peculiar feature of VDE cosmology, as other kinds of dynamical quintessence (Alimi et al. 2010) and coupled DE (Baldi et al. 2010) show completely different properties, with less power (in the former case) or a ΛCDM-type of behaviour (in the latter) on small scales. At higher and intermediate redshifts, ΛCDM-vde shows almost no differences from ΛCDM, as expected since the former is normalized to a lower initial value with respect to the latter and therefore needs to equal it before eventually overcoming it at smaller z values, as imposed by the larger σ_8 normalization. The effects of the different growth factor in this model start to become evident only at $z < 1$, where we see that the ratio of the $P(k)$ starts to increase. Whereas the ratio of VDE to ΛCDM for $k < 0.05 \, h \, \text{Mpc}^{-1}$ is substantially unaltered at all redshifts, small scales are affected by non-linear effects, eventually distorting its shape.

4.3 Halo abundance

In the following subsection, we will study the abundance of massive objects at different redshifts. Highlighting the differences arising among the three models in the different mass ranges, we want to study VDE's peculiar predictions for the massive cluster distribution and highlight its distinction from ΛCDM.

To this extent, we compare in Fig. 9 the three different mass functions at $z = 0$ computed for the $1 \, h^{-1}$ Gpc simulations versus the

ones obtained using the Tinker formula (Tinker et al. 2008). In the ΛCDM and ΛCDM-vde cases, the theoretical values are obtained using the standard parametrization, whereas in the VDE case we performed a non-linear fit of the mass function to the numerical data. We find that in the VDE case the four parameters of the Tinker mass functions take the values (assuming the standard notation) $A = 0.105$, $a = 0.75$, $b = 4.42$ and $c = 1.48$, thus differing substantially from the usual ones (which are $A = 0.187$, $a = 1.47$, $b = 2.57$ and $c = 1.19$). This difference is most likely due to a different value for the linear critical overdensity parameter δ_c; however, a complete understanding of this aspect would require a deeper knowledge of the linear perturbation theory in VDE cosmology, which is still under investigation.

In Fig. 10, we show the (cumulative) mass functions for the three models at $z = 0, 1, 2, 4$, as computed from the VDE-0.5, ΛCDM-0.5 and ΛCDM-0.5-vde simulations; the corresponding VDE-1, ΛCDM-1 and ΛCDM-vde-1 results can be found in Carlesi et al. (2011); they are not shown here again as they do not provide any new insights and rather confirm (and extend) the results to be drawn from the $500 \, h^{-1}$ Mpc boxes. We note that the VDE cosmology is characterized by a larger number of objects at all the mass scales and redshifts, outnumbering ΛCDM by a factor constantly larger than 2. In particular, this enhancement can be seen for the very large masses, where at low z the VDE/ΛCDM ratio reaches values of ~10. Although this value of the ratio seems to be a mere result of the cosmic variance, due to the low number of haloes found in this mass range, the computation of the mass function for the second $500 \, h^{-1}$ Mpc VDE realization and the $1 \, h^{-1}$ Gpc simulations makes us believe that the expected enhancement in this region must be at least a factor of 5.
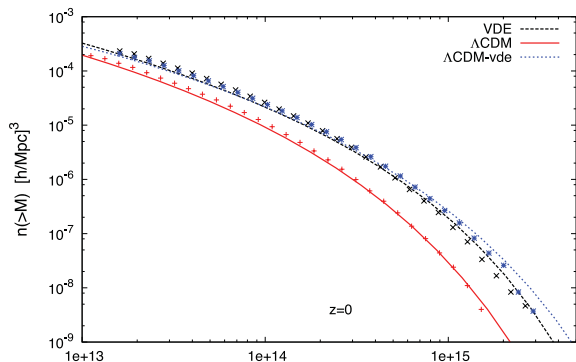
Interestingly enough, ΛCDM-vde has comparable characteristics to VDE, which leads us to the conclusion that the substantial enhancement in structure formation is mainly parameter driven, i.e. due to the overabundance of matter and higher normalization of matter density perturbations. Although this first observation may seem in contrast with what we have found in Section 4.2, where we have noted that VDE has less power on large scales in comparison to ΛCDM, we have to take into account that, in the hierarchical picture of structure formation, objects on small scales form first to subsequently give birth to larger ones. This means, in our case, that more power for large k-values should be regarded as an important
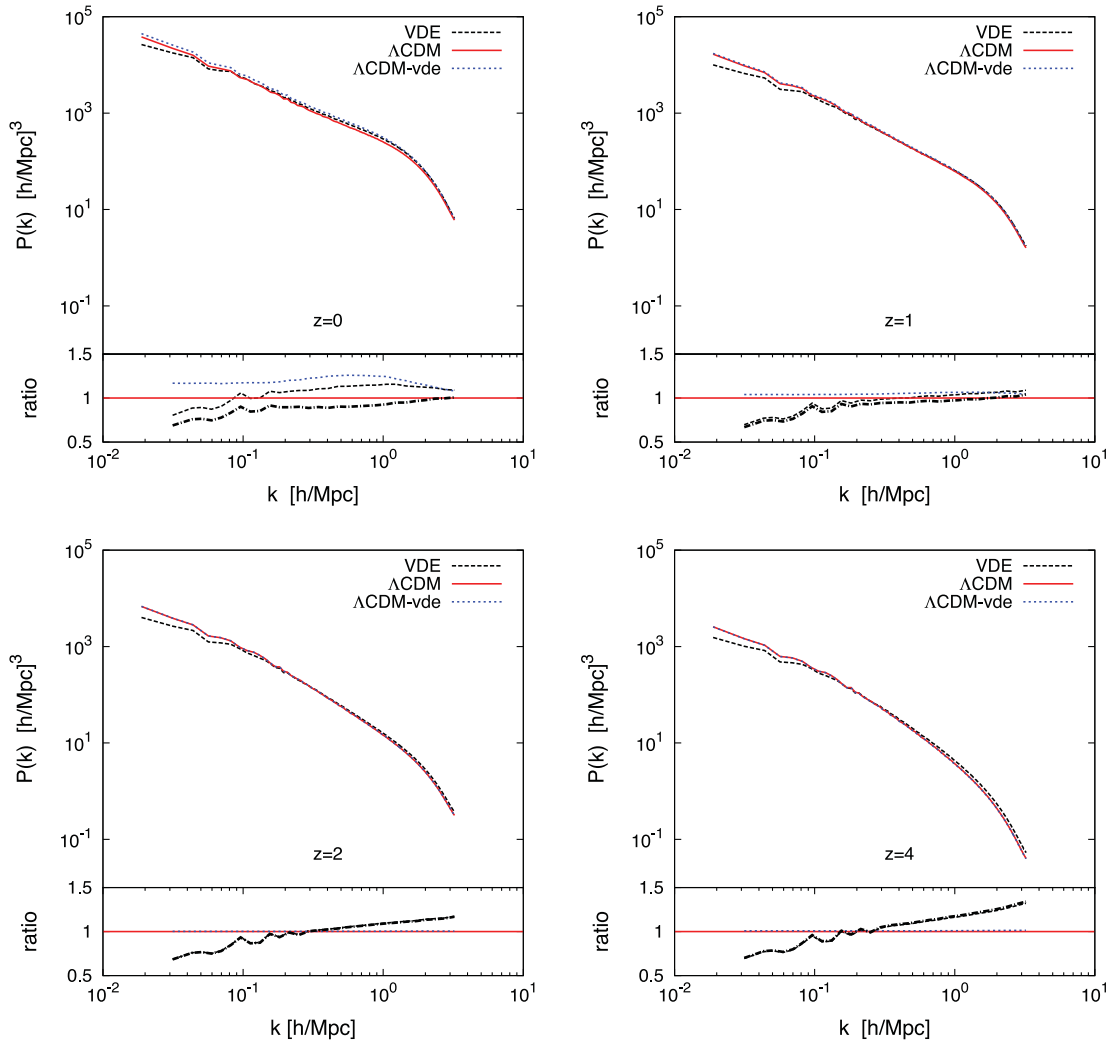
Figure 8. Power spectra at redshifts $z = 0, 1, 2, 4$; solid lines are for ΛCDM-0.5, dotted for ΛCDM-0.5-vde and dashed for VDE-0.5. The results from the $1\,h^{-1}$ Gpc simulations are not shown as they simply overlap with the present ones on the smaller-k end, without providing further insights on the small scales, where we expect non-linear effects to dominate.
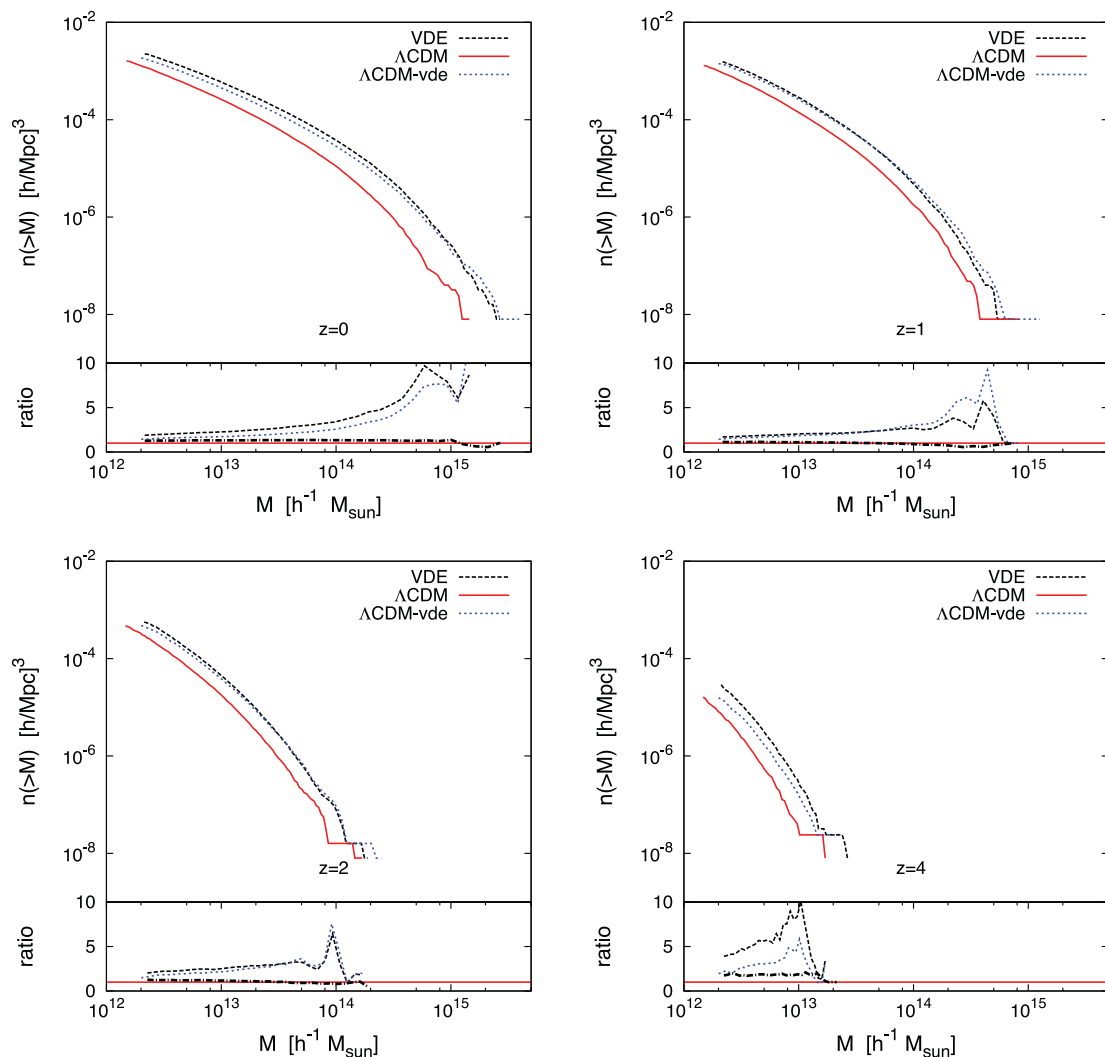
source of the overall enhancement together with the overabundance of matter, as already pointed out in the previous discussion. The evolution of the mass functions at different redshift allows us to disentangle the effect of the modified expansion rate; at higher red-

Figure 9. The numerical halo mass function for the three $1\,h^{-1}$ Gpc simulations at $z = 0$, showing the numerical results versus the Tinker theoretical values.

shift, in fact, both the ΛCDM and ΛCDM-vde mass functions are suppressed with respect to the VDE model, mostly because of the lack of power on small scales. These stronger initial fluctuations eventually trigger the earlier start of structure formation, but – as time passes – the effect of the increased expansion rate shown in Fig. 5 for the VDE cosmology suppresses structure growth, leading to a mass function below the ΛCDM-vde curve at around redshift 1. At this point, the VDE expansion rate starts decreasing with respect to the ΛCDM one, comparatively enhancing very large structure growth and eventually causing the two mass functions to be (nearly) indistinguishable at $z = 0$. In an attempt to disentangle further the effects of the new Ω_M from those due to the higher normalization of the matter power spectrum, we searched for a redshift z_0 at which ΛCDM and VDE have an identical σ_8 value, which would allow us to single out the impact of the different Ω_M parameter alone. Integrating numerically the power spectra of the different simulations' snapshots, we have found $z_0 = 0.18$, where σ_8 is 0.651 for both VDE and ΛCDM. Analysing the power spectra and mass functions at this redshift, we can conclude that the main effects of VDE, such as the overabundance of objects, are only due to the larger Ω_M, the impact of the different normalization of the matter fluctuations being practically negligible.

Figure 10. Mass function for ΛCDM(solid lines), VDE (dashed lines) and ΛCDM-vde (dotted lines) models at different redshifts, computed for the $500\,h^{-1}$ Mpc box simulations. We have also verified that the corresponding values computed for the $1\,h^{-1}$ Gpc simulations overlap to the ones shown here for $M > 10^{13}\,h^{-1}\,\mathrm{M}_\odot$, except for a smoother high-mass end. In the lower panels of the plots, VDE and ΛCDM-vde to ΛCDM ratios are represented by dotted lines while VDE to ΛCDM-vde are shown using dash-dotted lines.

Furthermore, if we look at Fig. 11, where we show the evolution with redshift of the number density of objects above the $M = 10^{14}\,h^{-1}\,\mathrm{M}_\odot$ threshold, we observe that the most massive structures in the two cosmologies form at comparable rates. This seems to suggest that in the VDE picture there is a subtle balance between the formation of new small haloes and their merging into more massive structures. Such an effect comes as no surprise if we again take into account that this model has two main opposite, different features that affect the formation of structures: a strong suppression on all scales induced by the faster expansion of the universe for a large redshift interval and an enhancement due to a higher density of matter and a larger power on the small scales.

An interesting consequence of this kind of behaviour is that the VDE overabundance of massive objects may address some recent observational tensions of ΛCDM, namely the high redshift of reionization and the presence of extremely massive clusters at $z > 1$. Recent microwave background observations seem to prefer a high reionization redshift, around $z \approx 10$ combined with a lower normalization of the matter perturbations, $\sigma_8 \approx 0.8$, whereas
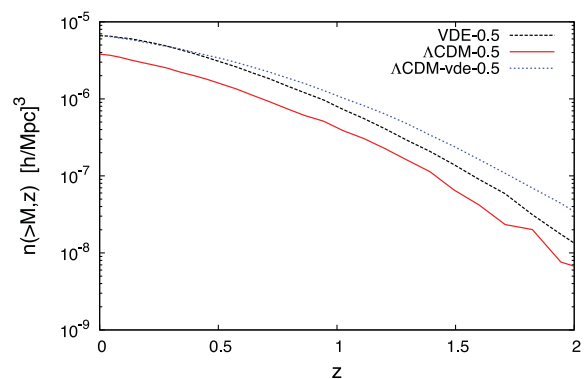
Figure 11. Number density evolution for objects more massive than $10^{14}\,h^{-1}\,\mathrm{M}_\odot$ as a function of redshift. The larger amount of massive clusters at higher redshift is a distinctive feature of VDE cosmology.

simulations have shown (see e.g. Raičević, Theuns & Lacey 2011) that early reionization can be achieved only for $\sigma_8 = 0.9$ or larger. In VDE, the appearance of dark matter haloes with masses larger than $10^{12} h^{-1} M_\odot$ as early as $z = 7$ (while equivalent structures appear in ΛCDM only for $z > 5$) might imply also a larger z_{reion}, provided the hierarchical picture of structure formation holds also in VDE at smaller mass scales. On the other hand, the existence of $M > 5 \times 10^{14} h^{-1} M_\odot$ clusters at $z > 1$ (as discussed in Jee et al. 2009; Brodwin et al. 2010; Foley et al. 2011) has also been considered by many authors (e.g. Baldi & Pettorino 2011; Enqvist et al. 2011; Hoyle et al. 2011; Baldi 2012) as a serious challenge to the standard ΛCDM paradigm; for a more thorough discussion of this issue in the context of VDE cosmology, we refer to aforementioned articles as well as Carlesi et al. (2011). However, the comparison to the ΛCDM-vde paradigm, also shown in Fig. 11, shows that VDE indeed acts as a source of suppression of structure growth with respect to the enhancement triggered by the increase in σ_8 and Ω_M. This effect is indeed a general result of uncoupled dynamical DE models (Grossi & Springel 2009; Li, Mota & Barrow 2011) as the presence of a larger fraction of DE at high z enhances Hubble expansion (as shown in Fig. 5), preventing a stronger clustering to take place.

In our case, it is also important to point out that the overprediction of objects at $z = 0$ may represent a shortcoming of the model, as observations on the cluster number mass function seem to be in contrast with such a prediction (see Vikhlinin et al. 2009; Wen, Han & Liu 2010; Burenin & Vikhlinin 2012). Furthermore, we have to keep in mind that these results assume a ΛCDM fiducial model, while the use of a different cosmology requires a careful handling of the data and does not allow a straightforward comparison to the observations, as they are affected by model-dependent quantities like comoving volumes and mass–temperature relations.

4.4 Void function

In order to identify voids, our void finder starts with a selection of point-like objects in three dimension. These objects can be haloes above a certain mass or a certain circular velocity or galaxies above a certain luminosity. Thus, the detected voids are characterized by this threshold mass, circular velocity or luminosity. Other void finders use different approaches (Colberg et al. 2008). The void-finding algorithm does not take into account periodic boundary conditions used in numerical simulations. Therefore, we have periodically extended the simulation box by $50 h^{-1}$ Mpc. In this extended box, we represent all haloes with a mass above the threshold of $5 \times 10^{12} h^{-1} M_\odot$ as a point. In this point distribution, we search at first the largest empty sphere which is completely inside the box. To find the other voids, we repeat this procedure, however taking into account the previously found voids. We allow newly detected voids to intersect with previously detected ones up to 25 per cent of the radius.

In Fig. 12, we show the cumulative number of voids with radius larger than R_{void}, the centre of which is in the original box. One can clearly see that for a given void radius there exist more voids in the ΛCDM than in the ΛCDM-vde and VDE models. The void distribution reflects the behaviour of the mass function shown in Fig. 10. At redshift $z = 0$, there exist less haloes with $m_h > 5 \times 10^{12} h^{-1} M_\odot$ in the ΛCDM model than in the other two models. Thus, on average larger voids are expected.
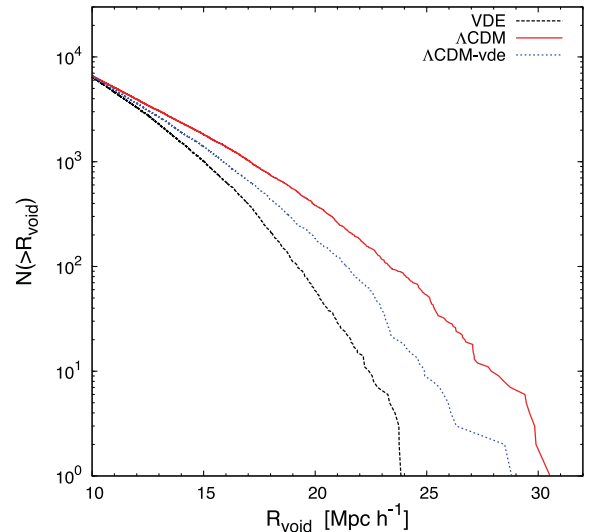

Figure 12. Void function for VDE-0.5, ΛCDM-0.5 and ΛCDM-vde-0.5 at $z = 0$. For the $500 h^{-1}$ Mpc box, we show the cumulative number of empty spheres of radius R which do not contain any object with mass larger than $5 \times 10^{12} h^{-1} M_\odot$.

4.5 Growth index

The growth of the perturbations can be related to the evolution of the matter density parameter by the general relation

$$\Omega_M^{\gamma(a)} = \frac{d \ln(\delta(a))}{d \ln(a)} . \qquad (19)$$

In the standard ΛCDM cosmology, the exponent $\gamma(a)$ can be approximated by a constant value $\gamma \sim 0.55$, although a more detailed calculation shows that this number is actually redshift dependent (see Bueno Belloso, García-Bellido & Sapone 2011). In Fig. 13, we show the evolution of this growth index $\gamma(z)$ computed from our VDE-0.5, ΛCDM-vde and ΛCDM-0.5 simulations. As expected, we do observe that in VDE structure formation is generally suppressed with respect to ΛCDM as an effect of the faster expansion rate. This statement is true until $z \approx 1.5$, when the ratio $H_{VDE}/H_{\Lambda CDM}$ starts decreasing, causing the steep increase in the growth index, eventually reducing again as soon as VDE enters into the phantom regime (see Section 2), undergoing an
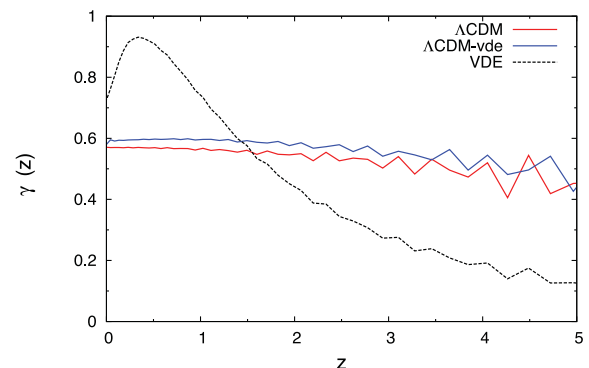
Figure 13. Growth index in the VDE and ΛCDM cosmologies from $z = 5$ to 0. Whereas ΛCDM's growth index has an almost constant behaviour with a mild dependence on the redshift, VDE changes dramatically from a regime where growth is relatively suppressed (until $z \approx 1.5$) to a relative enhancement at earlier times, where γ becomes larger.

accelerated expansion that strongly suppresses structure formation. This latter change, which takes place at $z \approx 0.5$, is reflected by the peak of $\gamma(z)$, which is reached for the same z. Actually, as stressed by different parametrizations (Bueno Belloso et al. 2011), the growth index is extremely sensitive to the value of the equation of state $\omega(z)$, although an explicit form in terms of VDE cosmology still has to be found. Indeed, the extremely different behaviour of this parameter at different redshifts is an interesting feature that clearly distinguishes the two models in a unique way. In fact, parameter-induced modification accounts for an ≈ 5 per cent change for the value of the growth factor, as the comparison between ΛCDM and ΛCDM-vde suggests. In this case, we observe a slight increase of the value of $\gamma(z)$ at all redshifts, due to the increased growth rate in ΛCDM-vde, also shown in Fig. 6. However, these changes have no impact on the shape of this function, which keeps its mild dependence on z unaltered. Therefore, $\gamma(z)$ can be effectively used as a tool for model selection, embodying effectively VDE's peculiar equation of state $\omega(z)$ and expansion history. Current observational bounds on γ constrain only weakly its value at high z values (see e.g. Nesseris & Perivolaropoulos 2008) or even favour a higher $\gamma(z = 0)$ (Basilakos 2012) in contrast to theoretical calculations based on ΛCDM. In any case, it will surely be something to be looked at in the near future, when deep surveys like *Euclid* (Laureijs et al. 2011) will provide stringent constraints on this quantity (Bueno Belloso et al. 2011).

5 DARK MATTER HALOES

In this section, we will discuss properties of (individual) haloes in VDE and ΛCDM. In particular, we will compare the distributions of masses, shape parameter, spin parameter, concentrations and formation redshifts as well as the shape of dark matter density profiles. In this way, we will determine the most important features that characterize on the average a single cosmological model. In addition, we are also cross-correlating haloes in the two models, studying differences on a one-to-one basis. With this we will be able to determine how the properties of a single given structure change when switching from one cosmological picture to the other.

5.1 General properties

To have a reliable description of the general halo properties, we need to properly select our sample from the catalogues, in order to include only those objects composed of a number of particle sufficient to resolve its internal structure without exceeding statistical uncertainty. Following Muñoz-Cuartas et al. (2011) and Prada et al. (2011), we set this number to approximately 500, even though other authors (see e.g. Bett et al. 2007; Macciò et al. 2007) suggest that lower values can be used, too. However, since we are dealing with different simulation runs with particles of different masses, the application of this criterion is not straightforward. In fact, since our aim is to compare *equivalent* structures (i.e. structures with the same M_{200}) and not structures composed by an identical number of particles, we need to choose our sample imposing a mass threshold M_{th}. For the simulations in the $500\,h^{-1}$ Mpc box, we have chosen $M_{th} = 5 \times 10^{13}\,h^{-1}$ M$_{\odot}$, which corresponds to haloes formed by at least 500 particles in VDE and ΛCDM-vde and 715 particles in ΛCDM; while for the larger $1000\,h^{-1}$ Mpc runs, we imposed an $M_{th} = 3 \times 10^{14}\,h^{-1}$ M$_{\odot}$ limit, i.e. 380 VDE and ΛCDM-vde particles and 545 ΛCDM ones. In the latter set of simulations, we see that we are also including haloes with an $\sim$20 per cent less than 500 particles in the VDE and ΛCDM-vde cases; this has been done

Table 2. Number of haloes above the mass (number) threshold M_{th} (N_{th}) per simulation. Also shown is the number of relaxed haloes, defined as those complying with the criterion introduced in Section 5.1.3.

| Simulation	M_{th} (h^{-1} M$_{\odot}$)	N_{th}	N_{total}	$N_{relaxed}$
ΛCDM-0.5	5×10^{13}	715	1704	1370
ΛCDM-vde-0.5	5×10^{13}	500	5898	5220
VDE-0.5	5×10^{13}	500	6274	5569
ΛCDM-1	3×10^{14}	545	4045	3533
ΛCDM-vde-1	3×10^{14}	380	9072	8117
VDE-1	3×10^{14}	380	12174	11508

since in the trade-off between resolution and sample size, we have felt more comfortable using a larger number of haloes at the expense of a slight reduction in accuracy, which will be none the less taken into account when analysing the results. The total number of haloes that comply with these conditions in every simulations, as well as the number of haloes that satisfy the relaxation criterion which will be discussed in Section 5.1.3, is shown in Table 2. The state of virialization of haloes will only be taken into account below when investigating the density profiles; for the study of the (distributions of the) two-point correlation functions, the spin and even the shape of haloes, we prefer to include even unrelaxed objects as they should clearly stick out in the distributions (if present in large quantities).

5.1.1 Correlation function

To study the clustering properties of the haloes in VDE cosmology, we computed the two-point correlation function using the definition

$$\xi(r) = \frac{V}{N^2} \sum_{i=1}^{N} \frac{n_i(r; \Delta r)}{v(r; \Delta r)} - 1, \qquad (20)$$

where N is the total number of objects above the given mass threshold in the simulation volume V, and n_i is the total number of objects within a shell of volume v and thickness Δr (of constant logarithmic spacing in r) centred at the ith object. In this case, we have limited our analysis to the $500\,h^{-1}$ Mpc boxes, ignoring the $1\,h^{-1}$ Gpc due to their lack of small-scale resolution. The results are plotted in Fig. 14, where we can see that the $\xi(r)$ is slightly smaller at all scales in VDE. Although in principle we would expect VDE cosmology to have an enhanced clustering pattern due to the increased distribution of massive objects observed in the mass function, the
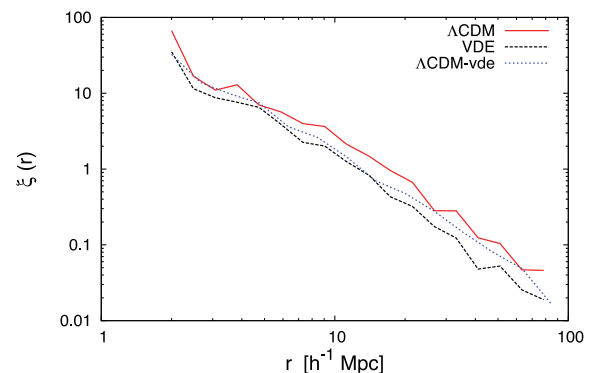
Figure 14. The two-point correlation function for objects more massive than $5 \times 10^{13}\,h^{-1}$ M$_{\odot}$ in the $500\,h^{-1}$ Mpc simulations.

Table 3. Best-fitting values for the mass–concentration relation for $z = 0$, obtained by fitting the relation given by equation (30) to the relaxed haloes concentrations and the two-point correlation function to a power law $(r_0/r)^\gamma$ for the ΛCDM, ΛCDM-vde and VDE cosmologies. r_0 values are given in h^{-1} Mpc.

Model	a	b	r_0	γ
ΛCDM	-0.115	2.11	13.4	-1.79
ΛCDM-vde	-0.112	2.21	12.1	-1.91
VDE	-0.098	2.17	10.1	-1.94

Figure 15. Spin parameter versus the analytical lognormal distribution calculated with the best-fitting parameters. The fit has been performed using the combined sample of haloes above $5 \times 10^{13}\,h^{-1}\,\mathrm{M}_\odot$ belonging to the three $500\,h^{-1}$ Mpc boxes, with those above the $3 \times 10^{14}\,h^{-1}\,\mathrm{M}_\odot$ limit in the $1\,h^{-1}$ Gpc boxes.

N^{-2} dependence of the two-point correlation function drags the total value down, making the final distribution function smaller than in ΛCDM. In fact, a similar behaviour can be observed for ΛCDM-vde, with a two-point correlation function below ΛCDM at practically all scales. In Table 3, we show the results of fitting $\xi(r)$ to a power law $(r_0/r)^\gamma$ from which we see that VDE is characterized by a smaller correlation length r_0 and a steeper slope γ.

5.1.2 Spin parameter, shape and triaxiality

Rotational properties of the haloes can be studied using the so-called spin parameter λ, a dimensionless number that measures the degree of rotational support of the halo. Following Bullock et al. (2001), we define it as

$$\lambda = \frac{L_{200}}{\sqrt{2} M_{200} V_{200} R_{200}}, \qquad (21)$$

where the quantities L (the total angular momentum), M (total mass), V (circular velocity) and R (radius) are all taken at the point where the average halo density becomes 200 times the critical density. Different authors have found (e.g. Barnes & Efstathiou 1987; Warren et al. 1992; Cole & Lacey 1996; Bullock et al. 2001; Gardner 2001; Macciò et al. 2007; Macciò, Dutton & van den Bosch 2008; Muñoz-Cuartas et al. 2011) that the distribution of this parameter is of lognormal type:

$$P(\lambda) = \frac{1}{\lambda \sigma_0^2 \sqrt{2\pi}} \exp\left[-\frac{\ln^2(\lambda/\lambda_0)}{2\sigma_0^2}\right], \qquad (22)$$

even though there are recent claims that this distribution has to be slightly modified (Bett et al. 2007).

Fitting the above function to our numerical sample by a non-linear Levenberg–Marquardt least-square fit, we find a remarkably good agreement, shown in Fig. 15 for the combined set of haloes of the $500\,h^{-1}$ Mpc and $1\,h^{-1}$ Gpc simulations. It is clear that the three models present no substantial difference in the values of these distributions, meaning that the change of cosmology has no impact on the rotational support of the dark matter structures.

The shape of three-dimensional haloes can be modelled as an ellipsoidal distribution of particles (Jing & Suto 2002; Allgood et al. 2006), characterized by the three axis $a \geq b \geq c$ computed by AHF as the eigenvalues of the inertia tensor

$$I_{i,j} = \sum_n x_{i,n} x_{j,n}, \qquad (23)$$

which is in turn obtained by summing over all the coordinates of the particles belonging to the halo.

We define the shape parameter s and the triaxiality parameter T as

$$s = \frac{c}{a}, \qquad T = \frac{a^2 - b^2}{a^2 - c^2}, \qquad (24)$$
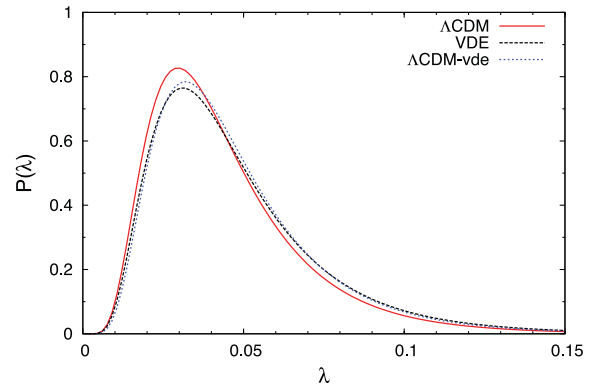
and we calculate the probability distributions $P(T)$ and $P(s)$ of the above parameters for all the objects above the aforementioned mass thresholds in our cosmological simulations to see whether the VDE picture of structure formation induces changes in the average shape and triaxiality. Similar to the previous case, we found again that halo shapes and triaxialities remain practically unaltered by VDE cosmology. This result could be expected, keeping in mind that VDE only affects background evolution. Once that structures start to form, detaching from the background evolution, they become affected by gravitational attraction only. Therefore, the internal structure of dark matter haloes remains generally unaltered by the presence of an uninteracting form of DE and cannot be used to discriminate between alternative cosmological paradigms. We have also verified that these results also hold when taking into account different halo samples separately, i.e. the massive ones of the $1\,h^{-1}$ Gpc simulations and the smaller ones belonging to the $500\,h^{-1}$ Mpc boxes.

5.1.3 Unrelaxed haloes

Before moving to the discussion of the properties of internal structure of the haloes, and in particular the density profile, we need to introduce and motivate a second criterion of selection for our halo sample, related to the degree of *relaxation* of the halo. An additional check is necessary since only a fraction of the structures identified in our catalogues completely satisfies the virial condition. In unvirialized structures, infalling matter and merger phenomena may occur, heavily affecting the halo shape and thus making the determination of radial density profiles and concentrations unreliable. In fact, unrelaxed haloes are most likely to differ from an idealized spherical or ellipsoidal shape since they have a highly asymmetric matter distribution, which in turn makes the determination of the halo centre an ill-defined problem, as discussed by Macciò et al. (2007) and Muñoz-Cuartas et al. (2011). Our halo finder AHF does not directly discriminate between virialized and unvirialized structures, giving catalogues containing both types of objects; however, it provides kinetic K and potential energy U for every halo identified, thus making the computation of the viral ratio $2K/|U|$ straightforward. Following one of the criteria used by Prada et al. (2011), we will consider as relaxed all the haloes satisfying the condition

$$\frac{2K}{|U|} - 1 < 0.5, \qquad (25)$$
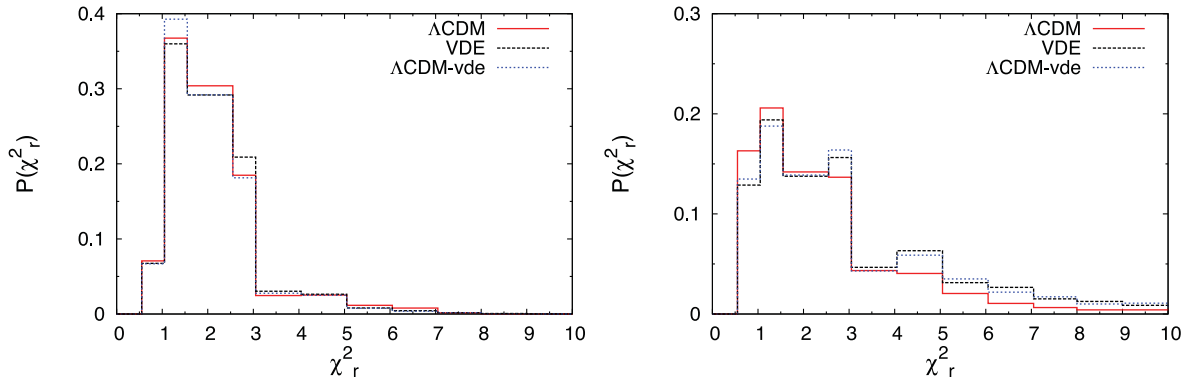
Figure 16. Reduced χ^2 distribution for the best fit to an NFW profile. On the vertical axis we plot the total fraction of haloes whose reduced χ^2 falls within the horizontal axis bin value. This is shown for relaxed haloes above the $5 \times 10^{13}\, h^{-1}\, M_\odot$ threshold belonging to the VDE-0.5, ΛCDM-vde-0.5 and ΛCDM-0.5 simulations (left-hand panel) as well as for those above the $3 \times 10^{14}\, h^{-1}\, M_\odot$ threshold belonging to VDE-1, ΛCDM-vde-1 and ΛCDM-1 (right-hand panel). The distributions show no particular difference among the three cosmologies; however, in the three $1\, h^{-1}$ Gpc simulations we note how lower resolution affects the χ^2 distribution, resulting in a thicker tail at higher values compared to the $500\, h^{-1}$ Mpc case, meaning that the fit to an NFW is on average worse.

without introducing additional parameters. Alternative ways of identifying unrelaxed structures can be found throughout the literature (e.g. Bett et al. 2007; Macciò et al. 2007; Neto et al. 2007; Knebe & Power 2008; Muñoz-Cuartas et al. 2011; Prada et al. 2011; Power, Knebe & Knollmann 2012), but since the results they give are qualitatively similar for reasons of computational speed and simplicity, we will not make use of them. The total number of haloes satisfying the relaxation condition is shown for every cosmology in Table 2.

5.1.4 Density profiles

N-body simulations have shown that dark matter haloes can be described by a Navarro–Frenk–White (NFW) profile (Navarro, Frenk & White 1996), which is given by

$$\rho(r) = \frac{\rho_0}{\frac{r}{r_{\rm s}}(1 + \frac{r}{r_{\rm s}})^2} , \qquad (26)$$

where the $r_{\rm s}$, the so-called scale radius, and the ρ_0 are in principle two free parameters that depend on the particular halo structure. However, ρ_0 can be written as a function of the critical density as $\rho_0 = \delta_{\rm c}\rho_{\rm c}$, where

$$\delta_{\rm c} = \frac{200}{3} \frac{c^3}{\log(1 + c) - \frac{c}{1+c}} ,$$

and $c = r_{\rm vir}/r_{\rm s}$ is the *concentration* of the halo relating the virial radius $r_{\rm v}(=r_{200}$ in our case) to the scale radius $r_{\rm s}$, which will be discussed in detail in the following subsection. This description is generally valid for ΛCDM, but simulations of ever increased resolution have actually revealed that the very central regions are not following the slope advocated by the NFW formula but rather follow a Sérsic or Einasto profile (cf. Navarro et al. 2004; Stadel et al. 2009).

Here we want to check to which degree the modified cosmological background affects the distribution of matter inside dark matter haloes, i.e. its density profile. All our (relaxed) objects in all the simulations have been fitted to equation (26), and to estimate the goodness of this fit we compute for each halo its corresponding χ^2, defined in the usual way:

$$\chi^2 = \sum_i \frac{\left(\rho_i^{\rm (th)} - \rho_i^{\rm (num)}\right)^2}{\Delta\rho_i^{\rm (num)}} , \qquad (27)$$

where the ρ_i are the numerical and theoretical overdensities in units of the critical density $\rho_{\rm c}$ at the *i*th radial bin and $\Delta\rho_i$ is the numerical Poissonian error on the numerical estimate. Since different halo profiles will be in general described by a different number of radial bins,[4] to make our comparison between different simulations and haloes consistent we need to use the reduced χ^2:

$$\chi_{\rm red}^2 = \frac{\chi^2}{N_{\rm pts} - N_{\rm dof} - 1} , \qquad (28)$$

where $N_{\rm pts}$ is the total number of points used (i.e. total number of radial bins) and $N_{\rm dof}$ is the number of degrees of freedom (free parameters).

The comparison of the distributions of the reduced χ^2 values for ΛCDM-vde, ΛCDM and VDE haloes belonging to the two set of $500\, h^{-1}$ Mpc and $1\, h^{-1}$ Gpc simulations, shown in Fig. 16, allows us to determine again that no substantial difference is induced by the VDE picture, for the same reasons discussed in the case of spin, shape and triaxiality distributions. The standard description of dark matter structures is thus not affected by the presence of a VDE.

5.1.5 Halo concentrations

In the last step of the analysis of the general properties of haloes, we will turn to concentrations, which characterize the halo inner density compared to the outer part. This parameter is usually defined as

$$c = \frac{r_{\rm vir}}{r_{\rm s}} , \qquad (29)$$

where $r_{\rm s}$ is the previously introduced scale radius, obtained through the best-fitting procedure of the density distribution to an NFW profile. We would like to remind that concentrations are correlated to the formation time of the halo, since structures that collapsed earlier tend to have a more compact centre due to the fact that it has more time to accrete matter from the outer parts. Dynamical DE cosmologies generically imply larger c values as a consequence of earlier structure formation, as found in works like those by Dolag et al. (2004), Bartelmann, Doran & Wetterich (2006) and Grossi & Springel (2009). In fact, since the presence of early DE usually

---

[4] Note that our halo finder AHF uses logarithmically spaced radial bins whose number depends on the halo mass, i.e. more massive haloes will be covered with more bins.

suppresses structure growth, in order to reproduce current observations we need to trigger an earlier start of the formation process, which on average yields a higher value for the halo concentrations. However, this result does not hold in the case of coupled DE, where the increased clustering strength induced by a fifth force sets a later start of structure formation, as discussed in Baldi et al. (2010).

In the hierarchical picture of structure formation, concentrations are usually inversely correlated to the halo mass as more massive objects form later; *N*-body simulations (Dolag et al. 2004; Muñoz-Cuartas et al. 2011; Prada et al. 2011) and observations (Comerford & Natarajan 2007; Okabe et al. 2010; Sereno & Zitrin 2012) have in fact shown that the relation between the two quantities can be written as a power law of the form

$$\log c = a(z) \log \left(\frac{M_{200}}{h^{-1} \, \mathrm{M}_\odot} \right) + b(z) , \qquad (30)$$

where $a(z)$ and $b(z)$ can have explicit parametrizations as functions of redshift and cosmology (see e.g. Neto et al. 2007; Muñoz-Cuartas et al. 2011; Prada et al. 2011). We can use our selected halo samples at $z = 0$ from the $500 \, h^{-1}$ Mpc and $1 \, h^{-1}$ Gpc simulations to obtain the $a(z = 0)$ and $b(z = 0)$ values for the ΛCDM, ΛCDM-vde and VDE cosmologies; the results of the best-fitting procedure to equation (30) are shown in Table 3.

These values are in good agreement with the ones found, for instance, by Dolag et al. (2004), Macciò et al. (2008) and Muñoz-Cuartas et al. (2011) [who quote for ΛCDM values of $a(z = 0) \approx -0.097$ and $b \approx 2.01$]; the $\sim$10 per cent discrepancy observed with their results is due to the fact that our results are obtained over a smaller mass range, 5×10^{13}–$2 \times 10^{15} \, h^{-1} \, \mathrm{M}_\odot$, whereas the previously cited works study it over an interval larger by more than three orders of magnitude, 10^{10}–$10^{15} \, h^{-1} \, \mathrm{M}_\odot$. Still, according to our results, the *c–M* relation for both the VDE and ΛCDM-vde cases is characterized by a shallower *a* exponent and a larger *b*. Although the magnitude of these changes is different in the two models, we can safely conclude that also in this case the results are mainly parameter driven, i.e. due to the larger value of Ω_M. Furthermore, the large error bars for $M > 10^{15} \, h^{-1} \, \mathrm{M}_\odot$ scales, due to the low statistics of massive haloes complying the relaxation requirements, make it difficult to determine to what extent the differences in the best-fitting relations among ΛCDM-vde and VDE could be eventually reduced in the presence of a larger sample.

We also need to mention that in our simulations the actual halo concentrations do not precisely follow equation (30) but rather scatter around it, as can be seen in Fig. 17, where the average *c* per mass bin is plotted against the corresponding best-fitting relations. This is not really surprising, since observations (Sereno & Zitrin 2012) and *N*-body simulations (Dolag et al. 2004) have shown that halo concentrations are lognormally distributed around their theoretical value calculated using equation (30). In Fig. 18, we show that this is indeed the case: the distribution of the $c(M)/c_{\mathrm{fit}}(M)$, where $c_{\mathrm{fit}}(M)$ is the theoretical concentration value for a halo of mass *M*, is extremely close to a lognormal one with an almost model-independent dispersion, $\sigma \approx 0.4$.

5.2 Cross-correlation

The next step in our analysis consists of studying the properties of the (most massive) cross-correlated objects found in the three models at $z = 0$. Whereas in the previous section our focus was on the distribution of halo properties, this time we aim at understanding how they change switching from one model to another.
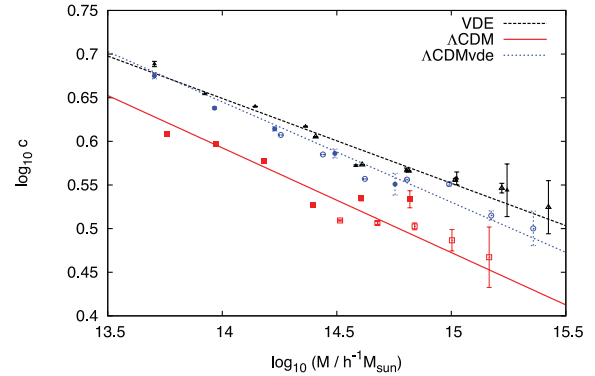
Figure 17. Best fit of the mass–concentration relation for the combined sample of relaxed haloes belonging to all the ΛCDM, ΛCDM-vde and VDE simulations. The points represent the average concentration values for the relaxed haloes in the corresponding mass bin; circles are for ΛCDM, triangles for ΛCDM-vde and squares for VDE. Empty dots stand for bins determined using haloes belonging to the $1 \, h^{-1}$ Gpc simulations, while filled ones refer to the $500 \, h^{-1}$ Mpc ones. The Poissonian error bars are computed using the number of selected haloes within each mass bin.
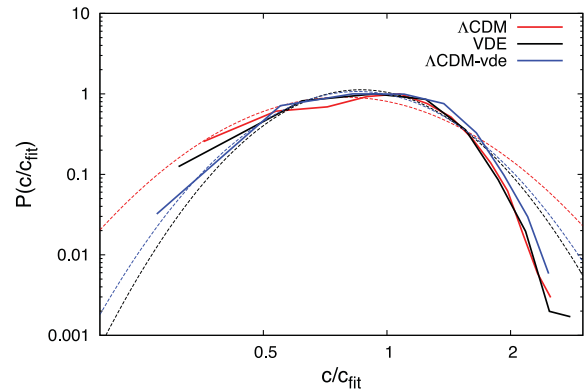

Figure 18. Distribution of the ratio between the actual concentration and the expected one (cf. equation 30) and its fit to a lognormal distribution.

The identification of 'sister haloes' among the different cosmologies can be done using the AHF tool `MergerTree`, which determines correlated structures by matching individual particles IDs in different simulation snapshots. For a more elaborate discussion of its mode of operation, we refer the reader to section 2.4 in Libeskind et al. (2010), where it has been described in greater detail. This time we decided to restrict our halo sample further by only picking the first 1000 most massive (ΛCDM) haloes. The criterion of halo relaxation has of course also been taken into account when dealing with profiles and concentrations.

5.2.1 Mass and spin parameter

In the two upper panels of Fig. 19, we show the ratios of the masses *M* and spin parameter λ for all the cross-correlated sets of simulations; in each panel we show the ratios for the $500 \, h^{-1}$ Mpc simulation boxes and the $1 \, h^{-1}$ Gpc ones. Both VDE and ΛCDM-vde show average mass and spin values scattered around values larger than 1 when compared to ΛCDM, whereas the cross-comparison of VDE to ΛCDM-vde shows average ratios close to unity at all mass scales. This substantial increase in the ratios is due to the earlier beginning of structure formation, triggered by the larger Ω_M and σ_8, as the comparison VDE/ΛCDM-vde shows. As we already did in
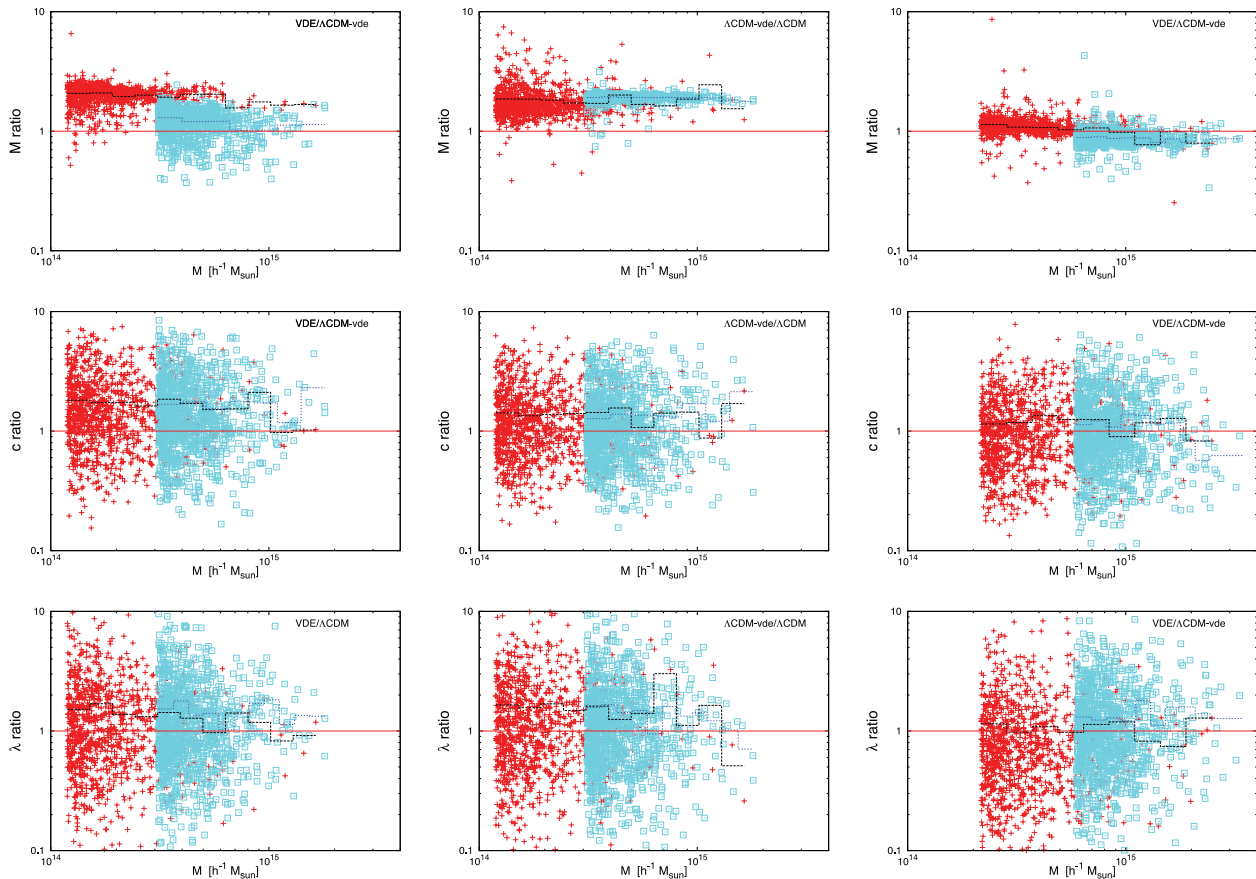
Figure 19. Mass and spin parameter correlation ratios for the first 1000 (relaxed and possibly unrelaxed) haloes. Panels on the left show the VDE/ΛCDM results and the ones in the centre show the ΛCDM-vde/ΛCDM results, while on the right the ratio VDE/ΛCDM-vde is plotted. Cross-identified objects are characterized by larger masses in VDE and ΛCDM-vde as a consequence of the higher Ω_M and σ_8 normalization value.

Section 5.1 when looking at the halo properties in general, we also conclude that when observing the same halo evolved under different cosmologies, the main effects are determined exclusively by the set of cosmological parameters chosen, the imprint of the cosmological background evolution being substantially negligible in this case. This makes the identification of a cosmic vector through the determination of halo properties impossible, since the background dynamics, which distinguishes VDE from any other non-interacting dynamical DE model, does not leave any observable imprint on these scales.

5.2.2 Halo concentrations and internal structure

As done in the previous section, in the determination of halo profiles and concentrations properties we discard unrelaxed haloes, but this time in a way so that our halo sample will still be composed of the first 1000 haloes satisfying condition given by equation (25). This same halo sample has also been used in the study of the M_{vir}–z_{form}, in order to be able to compare these results with the those obtained from concentrations consistently – although in principle formation redshifts are well defined even for unrelaxed haloes. Again, our procedure consists in fitting all the selected structure to an NFW profile, from which we will be able to derive the concentration parameter c and a measure for the quality of the fit χ^2; we will then compare these results in each cross-identified objects to see how a given halo structure changes when evolved under a different cosmology. Although not shown here, no particular trend in the

differences among ΛCDM, ΛCDM-vde and VDE pictures has been found for either NFW χ^2, shape or triaxiality, since in all the cases the ratios of these properties among cross-correlated haloes are centred around unity. Not surprisingly, we also find again a generally higher average value for the concentrations in VDE and ΛCDM-vde with respect to ΛCDM (see Fig. 19), a result which again can be explained by the larger value of Ω_M and σ_8. Similar concentrations for VDE and ΛCDM-vde haloes, shown in the upper right-hand panel of Fig. 19, can also be understood as a consequences of the similar masses of the haloes examined and the similar c–M relations found for the two cosmologies. However, even if from ΛCDM-vde cosmology we conclude that the different choice of Ω_M can explain in this case higher halo concentration, we need to remind that such a result is also a general feature of the dynamical nature of the DE fluid, as already found by Dolag et al. (2004), Bartelmann et al. (2006) and Grossi & Springel (2009).

6 CONCLUSIONS

In this work, we presented an in-depth analysis of the results of a series of N-body dark matter only simulations of the VDE cosmology proposed by Beltrán Jiménez & Maroto (2008). The main emphasis has been on the comparison to the standard ΛCDM paradigm, using a mirror simulation with identical number of particles, random seed for the initial conditions, box size and starting redshift. An additional series of simulations for a ΛCDM-vde cosmology has also been run using the VDE values for Ω_M and σ_8 within a standard

ΛCDM picture, to disentangle the effects of the parameter-induced modifications from the dynamical ones coming directly from the VDE model.

The use of a modified version of the GADGET-2 code required us to check the results with particular care. A consistency check of our simulations was performed by comparing the numerical results for the evolution of the growth factor to the analytical calculations, finding an excellent agreement between the two. We further had to adapt the halo-finding procedure, due to the fact that the critical density as a function of redshift $\rho_c(z)$, entering the definition of the halo edges, takes different values in VDE. Once halo catalogues had been obtained, we carried out our analysis at two different levels, namely

(i) we studied the very large-scale clustering pattern through the computation of matter power spectra, mass, void and two-point correlation functions and

(ii) we analysed halo structure, comparing statistical distributions and averages of spin parameters, concentrations, masses and shapes.

In the first point, making use of the full set of simulations, our analysis covered the whole masse range 10^{12}–10^{15} h^{-1} M$_\odot$ as well as different redshifts, so that we could make specific VDE model predictions for the number density evolution $n(>M, z)$ and growth index $\gamma(z)$. A distinctive behaviour, very far from the standard ΛCDM results, has been found for $\gamma(z)$ and, in particular, for the mass function that in VDE cosmology can be up to 10 times larger than the standard ΛCDM one. The latter result is due to the earlier onset of structure formation, and we have mentioned how it can be used to address current ΛCDM observational tensions with large clusters at $z > 1$ and possibly with early reionization epoch (cf. also Carlesi et al. 2011). At $z = 0$, we have shown that VDE cosmology requires the standard set of parameters entering the Tinker mass function to be modified; however, since the investigation of the linear perturbation theory is still ongoing, we lack the instruments to shed more light on this aspect.

Computing the cumulative mass function at different redshifts and making use of the ΛCDM-vde simulations, we have also observed how the condition $H_{VDE}(z) > H_{\Lambda CDM}(z)$, holding up to $z \approx 1$, induces a relative suppression of structure growth in this cosmological model, an effect that clashes with the increased matter density and σ_8. In fact, while on the one hand higher values of these parameters enhance the formation of a larger number of objects, on the other hand background dynamics suppresses clustering and growth. The interplay and relative size of these effects have been studied using the ΛCDM-vde simulations, showing that, for example, faster expansion in the past determines for VDE an expectation of clusters with $M > 10^{14}$ h^{-1} M$_\odot$ up to approximately five times smaller than what a simple increase in σ_8 and Ω_M would determine. This effect has been also seen in the void distribution, where suppression of clustering prevents small structures to merge into larger one and to rather spread in the field, so that underdense regions happen to be smaller and rarer than in ΛCDM and ΛCDM-vde. In these latter cosmologies, in fact, a higher contrast between populated and less populated regions is observed both in the power spectrum and in the colour-coded matter density.

In the second part of our work, we have focused on the study of internal halo structure. We found that VDE cosmology does not induce deviations in the functional form of the dark matter halo density profiles, which are still well described by an NFW (Navarro et al. 1996) profile, nor in the distributions for the concentrations and spin parameters, which are of the lognormal type as in ΛCDM. Shape and triaxiality are also unaffected: the distributions for the

relative parameters are identical and peaked at the same values in all the three cosmologies. The above results are a direct consequence of the fact that dark matter haloes, once detached from the general background evolution driven by the cosmic vector, evolve by means of gravitational attraction only, which is unaffected by the specific nature of DE. A net effect can be seen in masses, whose average values tend to be larger than in the ΛCDM case by a factor of ≈ 2, a straightforward consequence of the larger Ω_M and σ_8, as can be shown by a direct comparison of VDE to ΛCDM-vde results, which turn out extremely close in these cases. On the other hand, the different background evolution seems to affect c–M relations only slightly, changing the power-law index $a(z)$ and normalization $b(z)$ by 15 per cent. In this case, we have also found that these values in general agree with previous results from early DE studies such as those by Dolag et al. (2004), even though in this case it would certainly be necessary to test the relation down to smaller mass scales, where a better tuning of the parameter would also be possible, and with a larger statistics on the higher scales. However, in general, most of the halo-level effects which seem to characterize VDE can be simply explained in terms of the different cosmological parameters, as we did comparing these results to the outcomes of ΛCDM-vde simulations. For the first time then, through the results of the series of N-body simulations, we have shown that VDE cosmology provides a viable environment for structure formation, also alleviating some observational tensions emerging with ΛCDM. We have seen how the peculiar dynamics of this model leaves its imprint on structure formation and growth, and in particular how it affects predictions for large-scale clustering and halo properties. However, a close comparison of the deep non-linear regime results with different sets of observational data still needs to be performed, challenging us to improve the accuracy of our simulations and at the same time devise new and reliable tests which may shed some light not only on VDE but also on the nature of DE in general.

REFERENCES

Abazajian K. N. et al., 2009, ApJS, 182, 543
Alimi J.-M., Füzfa A., Boucher V., Rasera Y., Courtin J., Corasaniti P.-S., 2010, MNRAS, 401, 775

Allgood B., Flores R. A., Primack J. R., Kravtsov A. V., Wechsler R. H., Faltenbacher A., Bullock J. S., 2006, MNRAS, 367, 1781

Baldi M., 2012, MNRAS, 420, 430

Baldi M., Pettorino V., 2011, MNRAS, 412, L1

Baldi M., Pettorino V., Robbers G., Springel V., 2010, MNRAS, 403, 1684

Barnes J., Efstathiou G., 1987, ApJ, 319, 575

Bartelmann M., Doran M., Wetterich C., 2006, A&A, 454, 27

Basilakos S., 2012, preprint (arXiv:1202.1637)

Beltrán Jiménez J., Maroto A. L., 2008, Phys. Rev. D, 78, 063005

Beltrán Jiménez J., Lazkoz R., Maroto A. L., 2009, Phys. Rev. D, 80, 023004

Bett P., Eke V., Frenk C. S., Jenkins A., Helly J., Navarro J., 2007, MNRAS, 376, 215

Beutler F. et al., 2011, MNRAS, 416, 3017

Brodwin M. et al., 2010, ApJ, 721, 90

Bueno Belloso A., García-Bellido J., Sapone D., 2011, J. Cosmol. Astropart. Phys., 10, 10

Bullock J. S., Dekel A., Kolatt T. S., Kravtsov A. V., Klypin A. A., Porciani C., Primack J. R., 2001, ApJ, 555, 240

Burenin R. A., Vikhlinin A. A., 2012, preprint (arXiv:1202.2889)

Carlesi E., Knebe A., Yepes G., Gottlöber S., Jiménez J. B., Maroto A. L., 2011, MNRAS, 418, 2715

Colberg J. M. et al., 2008, MNRAS, 387, 933

Cole S., Lacey C., 1996, MNRAS, 281, 716

Comerford J. M., Natarajan P., 2007, MNRAS, 379, 190

Dolag K., Bartelmann M., Moscardini L., Perrotta F., Baccigalupi C., Meneghetti M., Tormen G., 2004, Modern Phys. Lett. A, 19, 1079

Enqvist K., Hotchkiss S., Taanila O., 2011, J. Cosmol. Astropart. Phys., 4, 17

Foley R. et al., 2011, ApJ, 731, 86

Gardner J. P., 2001, ApJ, 557, 616

Gill S. P. D., Knebe A., Gibson B. K., 2004, MNRAS, 351, 399

Grossi M., Springel V., 2009, MNRAS, 394, 1559

Guy J. et al., 2010, A&A, 523, A7

Hoyle B., Jimenez R., Verde L., 2011, Phys. Rev. D, 83, 103502

Huterer D., 2010, Gen. Relativ. Gravitation, 42, 2177

Jee M. et al., 2009, ApJ, 704, 672

Jimenez J. B., Maroto A. L., 2009, in AIP Conf. Proc. Vol. 1122, Physics and Mathematics of Gravitation. Am. Inst. Phys., New York, p. 107

Jing Y. P., Suto Y., 2002, ApJ, 574, 538

Knebe A., Power C., 2008, ApJ, 678, 621

Knebe A. et al., 2011, MNRAS, 415, 2293

Knollmann S. R., Knebe A., 2009, ApJS, 182, 608

Larson D. et al., 2011, ApJS, 192, 16

Laureijs R. et al., 2011, preprint (arXiv:1110.3193)

Lewis A., Challinor A., Lasenby A., 2000, ApJ, 538, 473

Li B., Barrow J. D., 2011, MNRAS, 413, 262

Li B., Mota D. F., Barrow J. D., 2011, ApJ, 728, 109

Libeskind N. I., Yepes G., Knebe A., Gottlöber S., Hoffman Y., Knollmann S. R., 2010, MNRAS, 401, 1889

Macciò A. V., Dutton A. A., van den Bosch F. C., Moore B., Potter D., Stadel J., 2007, MNRAS, 378, 55

Macciò A. V., Dutton A. A., van den Bosch F. C., 2008, MNRAS, 391, 1940

Muñoz-Cuartas J. C., Macciò A. V., Gottlöber S., Dutton A. A., 2011, MNRAS, 411, 584

Navarro J. F., Frenk C. S., White S. D. M., 1996, ApJ, 462, 563

Navarro J. F. et al., 2004, MNRAS, 349, 1039

Nesseris S., Perivolaropoulos L., 2008, Phys. Rev. D, 77, 023504

Neto A. F. et al., 2007, MNRAS, 381, 1450

Okabe N., Takada M., Umetsu K., Futamase T., Smith G. P., 2010, PASJ, 62, 811

Perlmutter S. et al., 1999, ApJ, 517, 565

Power C., Knebe A., Knollmann S. R., 2012, MNRAS, 419, 1576

Prada F., Klypin A. A., Cuesta A. J., Betancort-Rijo J. E., Primack J., 2011, preprint (arXiv:1104.5130)

Raičević M., Theuns T., Lacey C., 2011, MNRAS, 410, 775

Riess A. G. et al., 1998, AJ, 116, 1009

Sereno M., Zitrin A., 2012, MNRAS, 419, 3280

Sherwin B. D. et al., 2011, Phys. Rev. Lett., 107, 021302

Springel V., 2005, MNRAS, 364, 1105

Stadel J., Potter D., Moore B., Diemand J., Madau P., Zemp M., Kuhlen M., Quilis V., 2009, MNRAS, 398, L21

Tinker J., Kravtsov A. V., Klypin A., Abazajian K., Warren M., Yepes G., Gottlöber S., Holz D. E., 2008, ApJ, 688, 709

Vikhlinin A. et al., 2009, ApJ, 692, 1060

Warren M. S., Quinn P. J., Salmon J. K., Zurek W. H., 1992, ApJ, 399, 405

Wen Z. L., Han J. L., Liu F. S., 2010, MNRAS, 407, 533

Zeldovich Y. B., 1970, A&A, 5, 84

This paper has been typeset from a TEX/LATEX file prepared by the author.